



**CHALMERS**  
UNIVERSITY OF TECHNOLOGY

## **Fate of lead, copper, zinc and antimony during chemical looping gasification of automotive shredder residue**

Downloaded from: <https://research.chalmers.se>, 2024-03-13 10:10 UTC

Citation for the original published paper (version of record):

Stanivic, I., Cañete Vela, I., Backman, R. et al (2021). Fate of lead, copper, zinc and antimony during chemical looping gasification of automotive shredder residue. *Fuel*, 302. <http://dx.doi.org/10.1016/j.fuel.2021.121147>

N.B. When citing this work, cite the original published paper.



## Full Length Article

# Fate of lead, copper, zinc and antimony during chemical looping gasification of automotive shredder residue

Ivana Staničić<sup>a,\*</sup>, Isabel Cañete Vela<sup>a</sup>, Rainer Backman<sup>b</sup>, Jelena Maric<sup>a</sup>, Yu Cao<sup>c</sup>, Tobias Mattisson<sup>a</sup>

<sup>a</sup> Department of Space, Earth and Environment, Division of Energy Technology, Chalmers University of Technology, SE-412 96 Gothenburg, Sweden

<sup>b</sup> Department of Applied Physics and Electronics, Thermochemical Energy Conversion Laboratory, Umeå University, SE 901 87 Umeå, Sweden

<sup>c</sup> Department of Materials & Manufacturing Technology, Chalmers University of Technology, SE-412 96 Gothenburg, Sweden

## ARTICLE INFO

## Keywords:

Automotive shredder residue  
Chemical looping gasification  
Trace elements  
Ash characterization  
Fluidized bed  
Combustion

## ABSTRACT

Gasification experiments in this study were performed in a 2–4 MW indirect gasifier coupled to a semi-commercial CFB combustor at Chalmers University of Technology. Experiments were carried out during 13 days with automotive shredder residue (ASR), giving a unique opportunity to investigate the bed material under realistic conditions and with long residence times. The metal rich ash was accumulated in the bed, gaining some oxygen carrying capabilities, creating a chemical looping gasification (CLG) process. This study aims to expand the knowledge about the chemistry of zinc, copper, lead and antimony during CLG of ASR. Several experimental methods have been utilized, such as XRD, SEM-EDX and XPS along with detailed thermodynamic calculations to study chemical transformations that can occur in the system. Thermodynamic calculations showed that the reduction potential affect the phase distribution of these elements, where highly reduction conditions result in heavy metals dissolving in the slag phase. Copper and zinc ferrites, lead silicates and antimony oxides were identified at the particle surfaces in the bottom ash. The formation of an iron rich ash layer plays an important role, especially for copper and zinc speciation. The main pathways in the complex CLG system have been discussed in detail.

## 1. Introduction

In 2018 around 309 million motor vehicles were circulating in the EU [1]. The same year, the number of produced motor vehicles was around 19.2 million units corresponding to 20% of the global production [1]. Yearly there are around 6–8 million end-of-life vehicles (ELV) in the EU which generate around 7–8 million ton of waste. ELVs are processed in three main phases: depollution, dismantling and shredding [2]. Around 75 wt% of a dismantled vehicle is ferrous scrap metals and materials which can be mechanically recycled. The remaining 25%, which cannot be further separated or recycled is called Automotive Shredder Residue (ASR) corresponding to an amount of around 2 million tons yearly. Due to its heterogenous nature and complex composition ASR is largely landfilled [2].

The dismantling and recycling of ELVs are handled according to the European Directive 2000/53/EC. The European Directive 2000/53/EC requires EU members to recover or reuse end-of-life vehicles to a minimum of 95% and to recycle and reuse at least 85% average weight per

vehicle and year, starting from January 1st, 2015 [3]. This has provided an incentive for research and development of processes to divert ASR from being landfilled. According to the hierarchy of waste management, landfilling and incineration are the least desirable options. The focus should be to reduce production, reuse existing products and/or recycle material. Eventually, if none of aforementioned measures can be done, energy recovery is suggested [4]. Thermochemical processing of waste via gasification can be one way to recover chemicals, whereas hydrocarbons and syngas can be recovered and used in chemical and/or petrochemical industries. Dual fluidized bed (DFB) gasification is one technique which has been used for this purpose and is especially suitable for heterogenous fuels such as wastes [5–7].

The principle of DFB gasification is to use a bed material and two reactors, a combustor and a gasifier which are connected with loop seals. The bed material is circulated from the combustor, where it is heated, to the gasifier to supply enough heat for the endothermic gasification reaction. One technology based on DFB principle is chemical looping gasification (CLG). The bed material commonly used in CLG applications

\* Corresponding author.

E-mail address: [stanicic@chalmers.se](mailto:stanicic@chalmers.se) (I. Staničić).

<https://doi.org/10.1016/j.fuel.2021.121147>

Received 8 January 2021; Received in revised form 24 May 2021; Accepted 27 May 2021

Available online 12 June 2021

0016-2361/© 2021 The Author(s). Published by Elsevier Ltd. This is an open access article under the CC BY license (<http://creativecommons.org/licenses/by/4.0/>).

consist of metal oxides and is referred to as oxygen carriers. Examples of metal oxides which have been used as oxygen carriers are ilmenite, hematite and steel converter slag [8–11]. Together with the gasifying agent the oxygen carriers will provide the necessary oxygen to partially oxidize the fuel. The produced raw gas can be used for heat and power production or synthesized into various fuels [12]. Thermal conversion of ASR into valuable products, such as syngas and hydrocarbons, has been investigated in the Chalmers Research Unit showing the production of valuable gas [13,14]. The high ash content of the fuel, will result in an increased ash fraction in the bed material as the fuel is used, and the high metal content may mean that the bed will exhibit behaviors similar to oxygen carriers, i.e. oxygen carrier transfer.

Several studies have been conducted on gasification of biomass and the influence of the ash components on different bed materials. Silica sand for example which has been used for biomass gasification have shown to form a calcium and magnesium rich surface layer and potassium rich inner layer [15]. However, the use of sand as bed material may induce formation of potassium silicates with low melting temperatures [16]. Olivine on the other hand does not form melts to the same extent and has shown to increase defluidisation time compared to silica sand [17,18]. In order for olivine to operate optimally it must undergo an “activation” process, which includes an ash layer formation [19]. This involves formation of a calcium rich layer, migration of iron to the surface of the particle and interaction with ash components [20–22]. The formation of an ash layer has been investigated by several researchers [15,21,23,24]. During biomass gasification potassium enrichments have been observed in the formed cracks of olivine particles [24] along with calcium rich outer layer [15]. However, studies also report magnesium to cover the surface along with elevated amounts of iron [15]. The elevated amount of iron could imply oxygen carrying capabilities of the bed material [24–26].

ASR consists of glass, fibers, rubbers, foams, wood, metals and a variety of plastics. The high metal content in ASR could contain significant fractions of Fe, Al, Cu, Zn, Pb, Cr and Ni which affects the composition of the ashes and hence the possibilities for disposal [27,28]. There are several drawbacks regarding disposal of these ashes. One example is the loss of natural and monetary resources. Another example is the environmental effect that hazardous content may have [27]. Elements of interest that are enriched in the ASR fraction are Pb, Sb, Cu and Zn. Lead is commonly used as stabilizer in plastics, electronics and wires and may be released during combustion, either to the gas phase to end up in the fly ashes or interact with the bed material. Antimony in the form of antimony trioxide is for example used as flame retardant substance in seat covers. Zinc is commonly used in applications involving casting, coating, door handles and locks. The major source of copper is from the wiring and electrical components. The content of these elements in ASR-ash could reach levels around one weight percent. The literature around trace element behavior in biomass gasification is scarce and most of the literature concern coal [29,30]. Research conducted around these elements during normal combustion and gasification are often associated with intrinsic volatility of species. In fluidized beds a high flux of bed material may lead to heavy metals combining into condensed solution, either with the bed or ash particles [31,32]. Studies on the fate of alkali and trace elements have been described in biomass gasification [33,34]. One common approach has been to utilize thermodynamic calculations to study the behavior of trace elements [16,35]. However, no experimental investigations are available regarding interaction of trace elements with bed materials during chemical looping gasification of ASR.

This study aims to expand the knowledge about the chemistry of copper, lead, zinc and antimony in chemical looping gasification of ASR. Possible pathways of these elements in the CLG system will be discussed. For this purpose, both experimental and theoretical studies will be performed where the influence of ash content and temperature is investigated. The main experiments were carried out using a 2–4 MW indirect gasifier at Chalmers University of Technology which is coupled

to a semi-commercial CFB combustor. Bottom ashes extracted from the combustor and loop seals will be characterized along with the fly ash obtained from the secondary cyclone. Thermodynamic calculations will be used to provide information regarding the different behavior in the gasifier and combustor and will be used for comparison with the experimental investigation.

## 2. Experimental section

Bed and ash samples were obtained from experiments performed in the Chalmers Research Unit, which is a semi-commercial plant composed of a 10–12 MW<sub>th</sub> circulating fluidized bed combustor and 2–4 MW<sub>th</sub> bubbling bed gasifier. The layout and sampling points are presented in Fig. 1. Bed material circulates between the gasifier (6) and combustor (2) via particle distributor (4) and two loop seals (5) and (7). Steam gasification of three different ASR batches (8) was carried out at temperatures between 790 and 840 °C. As the unit has research purpose, the produced raw gas from the gasifier is not utilized as it would be in a commercial plant, but instead re-directed to the boiler where it is combusted [14]. The heat produced in the process is used for heating up Chalmers campus. Wood chips is the fuel fed to the combustor (1), which operates at a temperature above 850 °C. Bed material, olivine sand, is heated up in the combustor via exothermic combusting process and circulated to the gasifier where heat is released enabling endothermic gasification reaction of ASR. The flue gases from the combustor pass through a cyclone (3) to remove fly ash. A secondary cyclone (9) removes finer particles before entering the textile filter (10). Lime is added before the textile filter (10).

The gasifier was operated daily for 10 h during weekdays for a total of 13 days, while the combustor was in continuous operation. The mean process parameters for the last day are presented in Table 1. Information regarding variation in operating conditions and parameter study is reported by Pissot et al. [14]. A summary of the measurement range of the operating parameters is presented in Table S1 in Supplementary Material.

The olivine bed was replaced in small parts where addition and removal of the bed was made only to regulate the pressure drop in the combustor. During the experimental campaign K<sub>2</sub>CO<sub>3</sub>, K<sub>2</sub>SO<sub>4</sub> and CaCO<sub>3</sub> additions were made to the bed. Approximately 2.5 kg K<sub>2</sub>CO<sub>3</sub> was added on the first day in order to activate the olivine bed. Thereafter 3 kg K<sub>2</sub>CO<sub>3</sub> and 1 kg K<sub>2</sub>SO<sub>4</sub> were added on day 4 for the same purpose. On day 11 a test was performed by adding 2.5 kg CaCO<sub>3</sub> to the gasifier to see the effect on the formed dioxins. Ash was accumulated in the bed as the olivine bed was only replaced in small parts. The ash originates mainly from ASR which is composed of 32–47 wt% ash, see Table 2, while ashes from wood pellets have significantly lower ash content, below 0.7 wt%. Three different ASR fuel batches were used in the experimental campaign, the feeding days are indicated in Table 2. The elemental composition and fuel analysis were carried out by the Research Institutes of Sweden (RISE). The total moisture content and ash content in the fuel was determined according to SS-EN-ISO 18134–2 and SS-EN-ISO 18122 respectively. The main elements Al, Si, Fe, Ti, Mn, Mg, Ca, Ba, Na, K and P were determined according to ASTM D 3682 while the trace elements As, Pb, Cd, Cr, Cu, Co, Ni, Zn, V and Mo were determined according to ASTM D 3683, analyzed with ICP-OES. The corresponding ASR ash composition can be found in Table S2 in Supplementary Material.

### 2.1. Characterization techniques

Crystalline phases in bed samples extracted from the process were determined by X-ray Powder Diffraction (XRD) using the Bruker D8 Advanced system with CuKα1 radiation. The samples were pre-treated by light crushing in a mortar. The diffractometer was collected at 2θ range of 20–80°. A step size of 0.02° and counting time 2 s/step were used.

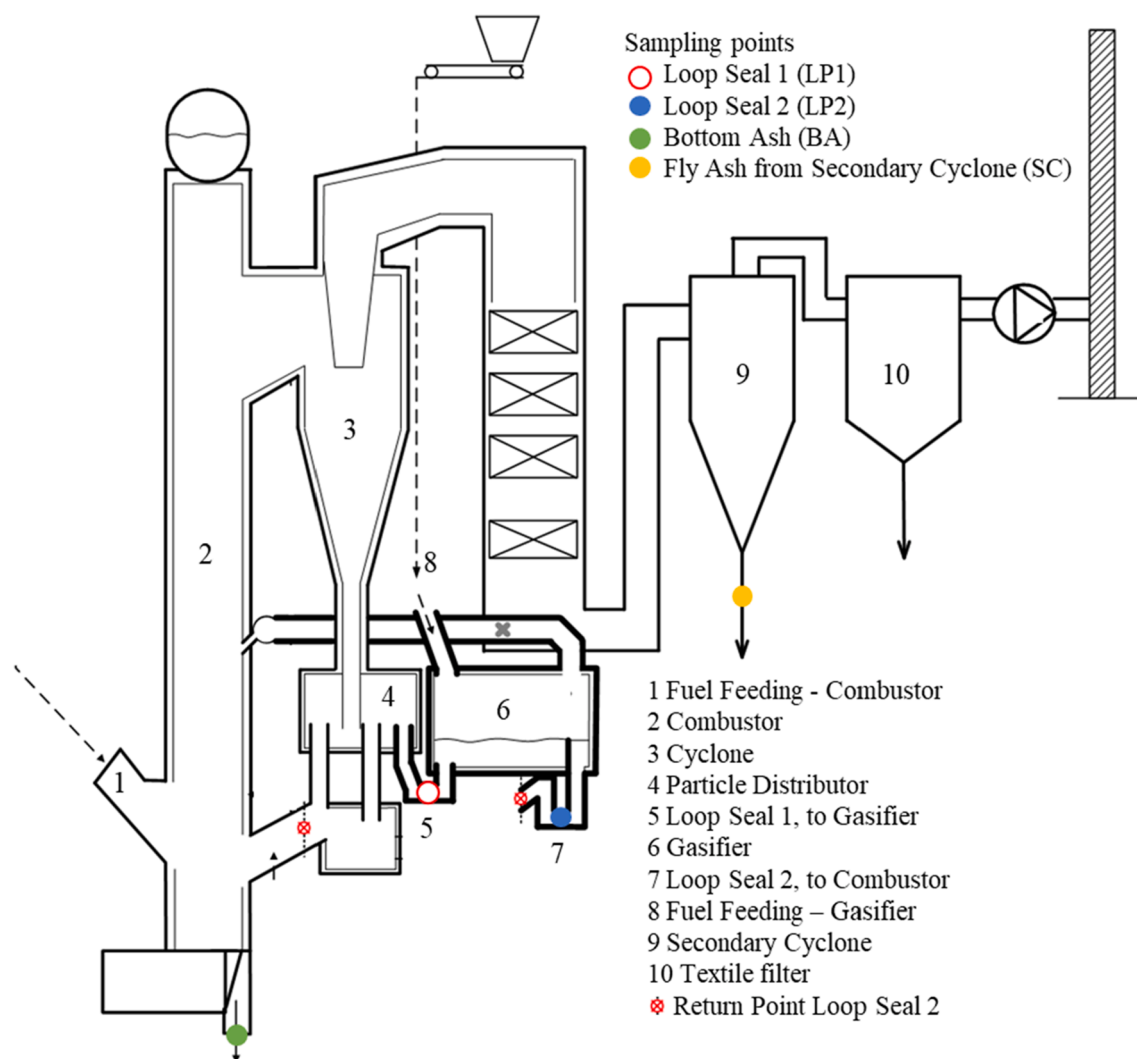


**Fig. 1.** Illustration of Chalmers dual fluidized bed system. The red symbol represents the connection between loop seal 2 and return to the combustor. Solid sampling points are indicated in the figure. (For interpretation of the references to colour in this figure legend, the reader is referred to the web version of this article.)

**Table 1**  
 Mean operational parameters for day 13, the last day of experiments.

Temperature in combustor	Temperature in gasifier	Temperature of raw gas	Fuel flow in combustor	Fuel flow in gasifier	Air fluidization in combustor	Steam fluidization in gasifier	Circulation rate
870 °C	830 °C	750 °C	1750 kg/h	270 kg/h	9600 kg/h	160 kg/h	20 000 kg/h

Morphology of the particles surface was examined using Scanning Electron Microscope (SEM), where Quanta 200 ESEM FEG from FEI was used. The instrument is equipped with an Oxford Inca Energy Dispersive X-ray (EDX) system for chemical analysis. Samples were mounted on carbon tape to study the particle surfaces. Cross section analysis was also performed. For this specific investigation, samples had to be prepared by molding the samples in epoxy. The samples were thereafter polished before being analyzed.

X-ray Photoelectron Spectroscopy (XPS) was used for surface material characterization which provided elemental and chemical information for solid samples. PHI 5000 VersaProbe III Scanning XPS Microprobe (Base pressure of  $1 \times 10^{-9}$  bar) has been used with monochromatic Al-source (25 W). Dual beam flood of low-energy electrons and low-energy argon ions were used to provide charge neutralization. Spectra were recorded with a 100  $\mu\text{m}$  beam size and pass energy of 224 eV and 26 eV for surveys and high-resolution spectra respectively. Several point analyses were performed on different particles in each

fraction. The high-resolution spectrum obtained were fitted using Multipak software (version 9.7.0.1) with a Shirley background and Gaussian/Lorentzian line shape. NIST database was used to identify possible compounds [36]. Binding energies were referenced by setting adventitious carbon C1s peak to 284.8 eV [36–38]. Peak constraints regarding area ratios and spin-orbit separation were defined based on literature [38]. The chemical states are compared with experimental data reported in literature using similar experimental settings.

## 2.2. Thermodynamic equilibrium calculations

FactSage 7.2® software was used for thermodynamic equilibrium calculations [39]. Both global and local calculations are performed. Global calculations are performed to study the behavior of Pb, Cu and Zn in the gasifier and combustor. The local thermodynamic calculations are based on the surface speciation as obtained from the quantification procedure from the x-ray photoelectron spectroscopy, and has been used



**Table 2**

Proximate and ultimate analyses of the three ASR fuel batches used in this work. Main ash components along with copper, lead, antimony and zinc concentrations reported in the table [14].

	Unit	Batch 1	Batch 2	Batch 3
Feeding day		1	5	12
Moisture	wt%	0.9	0.5	0.4
Ash	wt%	46	37	32
C	wt% daf	33	42	47
H	wt% daf	4.3	5.0	5.4
N	wt% daf	1.3	1.5	1.6
S	wt% daf	0.33	0.24	0.19
Cl	wt% daf	0.5	0.63	0.64
Al	wt%	2.4	1.6	1.5
Si	wt%	6.6	4.8	4.2
Fe	wt%	11	8.3	6.8
Mg	wt%	0.68	0.51	0.48
Ca	wt%	2.9	2.3	2.1
Na	wt%	0.77	0.59	0.49
K	wt%	0.41	0.34	0.33
Cu	mg/kg	5 500	5 800	5 500
Pb	mg/kg	1 100	600	600
Zn	mg/kg	22 000	15 500	13 800
Sb	mg/kg	190	1200	1400

previously for analysis of trace elements on oxygen carrier particles [40]. The local calculations are used to study chemical speciation on the surface of the bed particles. The relation between the abbreviations, phases and constituents used in this paper are presented in Table 3.

### 2.2.1. Effect of increasing ash content

The module *Equilib* was used together with the databases FactPS, FTToxid, FTSalt and HSCA. The latter is a database which consists of data with additional gases and solids originating from HSC Chemistry 9 [41]. More specifically the database includes compounds of As, Co, Cr, Cu, Mn, Ni, Pb, Sb, V and Zn and is thus believed to improve the quality of the calculation with respect to these species.

Input parameters were chosen based on elemental composition of fuel, see Table 2, and loop seals together with mean values of mass flows and temperatures, Table 1. The partial pressure of O<sub>2</sub> was monitored during the process and specified in the calculations to 0.05 atm in the combustor and 0.00001 atm in the gasifier. The output provides equilibrium compositions of the gas, solids and solid solutions. The calculations were performed in two steps. First the gasifier is simulated (blue box in Fig. 2) using ASR fuel, fluidizing steam and the experimentally determined bed composition in the loop seals as input streams. The calculation was performed at atmospheric pressure and 830 °C, the resulting phases were transferred to an oxidizing environment corresponding to the environment in the combustor (red box in Fig. 2). The second calculation was performed at atmospheric pressure and 870 °C.

**Table 3**

List of abbreviations of phases and their major phase constituents in this paper.

Abbreviation	Phase	Phase constituents
OlivA	Olivine	(Ca,Mg,Fe,Zn) <sub>2</sub> SiO <sub>4</sub>
cPyra	Clinopyroxene	(Ca,Mg,Fe,Al,Si) <sub>3</sub> SiO <sub>6</sub>
Feldspar	Feldspar	(K,Na)AlSi <sub>3</sub> O <sub>8</sub>
Neph	Nepheline	(K,Na)AlSiO <sub>4</sub>
Mela	Melilite	(Ca,Pb) <sub>2</sub> (Mg,Fe,Zn)Si <sub>2</sub> O <sub>7</sub>
SPINA	Spinel	(Fe,Mg,Al,Zn) <sub>3</sub> O <sub>4</sub>
SlagA	Slag	SiO <sub>2</sub> , (K,Na)AlO <sub>2</sub> , (Mg, Ca, Na <sub>2</sub> , K <sub>2</sub> , Cu <sub>2</sub> , Pb, Zn)O
SaltF	Salt	(Na,K) <sub>2</sub> SO <sub>4</sub> (Na,K)Cl
MeOA	Metal oxide	(Fe,Zn,Ca,Mg)O
Solids	Stoichiometric solids	CuFe <sub>2</sub> O <sub>4</sub> Cu <sub>2</sub> Fe <sub>2</sub> O <sub>4</sub> FecO <sub>4</sub> BaMg <sub>2</sub> Si <sub>2</sub> O <sub>7</sub> BaSO <sub>4</sub> PbTiO <sub>3</sub>

The calculations consisted of 1987 species in total, 98 solutions and 794 phases. These two calculation steps were repeated five times, for five different days with different ash contents.

**2.2.1.1. Effect of reduction potential.** The effect of the reduction potential is investigated using data from the last day of experiments, day 13. Different partial pressures of oxygen are investigated corresponding to different reduction potentials in the dual fluidized beds. The reduction potential, defined as the logarithmic ratio  $\log_{10}[p_{\text{CO}}/p_{\text{CO}_2}]$  ranges from  $-8.3$  to  $-0.8$  which corresponds to oxygen partial pressures between  $0.21$  and  $10^{-16}$  atm, a range which is of relevance for the particles during combustion. This provides insights of compound formation in different regions of the dual fluidized beds as the local availability of oxygen may differ. Furthermore, higher reduction potentials could also provide information about the insides of the particles since the oxygen availability decreases further into the particles.

## 3. Results

Four samples were extracted from the bottom of the combustor side (2), the loop seals before (5) and after (7) the gasifier and the fly ash from the secondary cyclone (9), see Fig. 1. All samples were extracted on the last day of the gasifier operation, day 13. The elemental composition of these samples is provided in Table 4, which were all analysed by Research Institutes of Sweden (RISE) except for the reference case. The reference case, fresh olivine was analysed by ALS Scandinavia and is used for comparison.

The elemental composition in loop seals for day 1–3, 5 and 13 are summarized in Fig. 3. For the first day, elemental analysis of loop seal 2 is presented as the elemental composition in LP1 and LP2 are similar, see Table 4. The left figure shows the main ash components Mg, Si, Fe, Ca, K and Al. The right figure shows the content of minor elements Cu, Pb, Sb and Zn with the content of Zn on the secondary y-axis.

The results for the fly ash are summarized in Fig. 4. Both the bed composition in loop seal 1 the fly ash from the secondary cyclone show a decrease of Mg relative to other elements, as the amount of ash increases with time. The amounts of Si stay at the same level. The minor elements show a constant increase as a function of time. Both Zn and Cu show similar behavior following the Fe and Al-increase. The Sb concentration also increases while Pb remains somewhat constant. Fig. 4 below shows the elemental composition of the fly ash as a function of time where a steep increase of Fe and Al is observed along with Zn.

### 3.1. Thermodynamic equilibrium calculations

#### 3.1.1. Effect of increasing ash content

The main phase distribution for both the gasifier and combustor over time, based on the elemental analyses and mass flows, are presented in Fig. 5. In total five calculations were performed for day 1–3, 5 and 13 as indicated in the figure. The variation is not large between days although a trend of decreasing amount of olivine and nepheline may be observed as well as an increase of spinel and clinopyroxene, see Table 3 for explanation of the phases. Some feldspar is formed at the expense of nepheline. The results do not indicate any major phase transition between the combustor and gasifier. This is likely due to the large amount of olivine which does not have oxygen carrying capability but could also depend on that the oxidation potential is not low enough in the gasifier to reduce the material further. However, locally the oxygen availability could be higher ( $p(\text{O}_2) = 0.21$  atm) in the combustor which could oxidize certain phases in the bed, for example Fe<sub>3</sub>O<sub>4</sub> to Fe<sub>2</sub>O<sub>3</sub>. Fig. 5 shows that olivine is the major phase in both reactors. Fig. 5 also shows that a slag phase (SlagA) is formed in both the gasifier and combustor for the first day. The slag phase consists of a major part SiO<sub>2</sub> along with lower concentrations of MgO, CaO, KAlO<sub>2</sub>, NaAlO<sub>2</sub>, PbO and Cu<sub>2</sub>O. In the combustor small amount of slag is formed again on day 5,

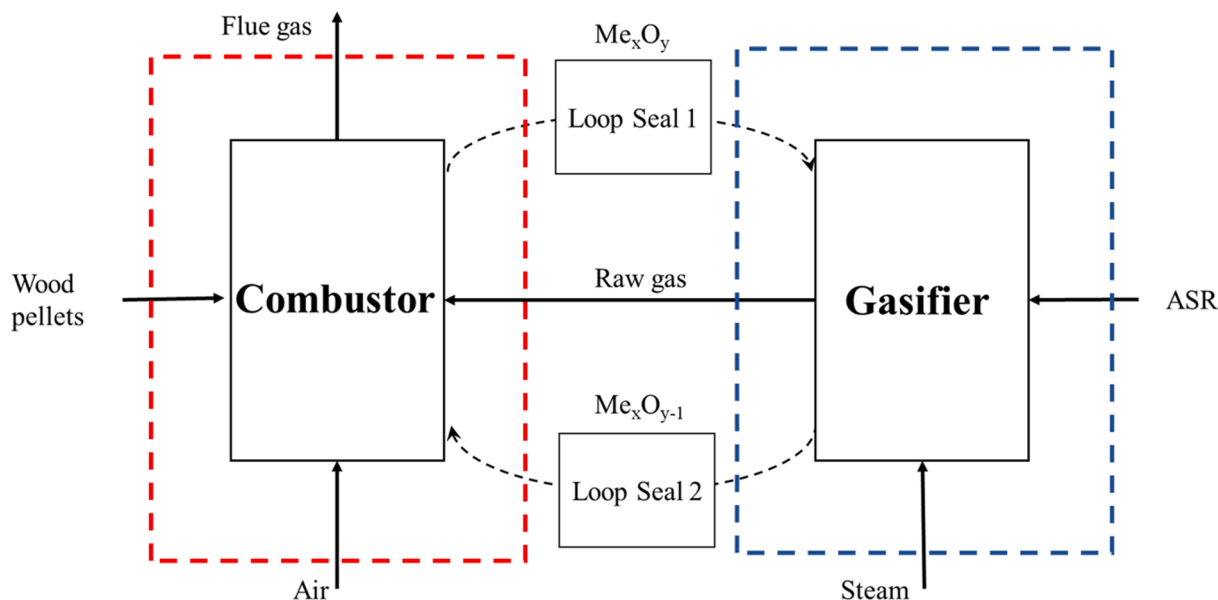


Fig. 2. Simplified illustration of the experimental setup at Chalmers and overview of the thermodynamic calculations.

Table 4

Elemental analyses along with acronyms of fresh olivine and ashes sampled on the last day of operation, day 13.

Specie	Unit	Origin	Fresh olivine	Bottom Ash	Loop Seal 1	Loop Seal 2	Fly Ash
		Acronym	REF	BA	LP1	LP2	SC
Al	wt% dry		0.30	0.93	1.6	1.6	4.4
Si	wt% dry		37.7	17	18	18	14
Fe	wt% dry		6.8	7.0	7.7	7.7	21
Mg	wt% dry		46.9	21	18	19	2.7
Ca	wt% dry		<0.08	6.2	7.1	7.3	8.4
Na	wt% dry		<0.05	0.6	0.59	0.64	1.3
K	wt% dry		<0.09	1.7	1.7	1.8	2.6
Cu	mg/kg dry		2.9	3 400	3 800	3 400	12
							000
Pb	mg/kg dry		<1	340	430	420	1 200
Zn	mg/kg dry		28	10 000	14 000	14	36
						600	000
Sb	mg/kg dry		–	650	1 500	1 500	2600

corresponding to 0.02 wt% of the total solid phases. In the gasifier the slag phase occupies 0.04 wt% on day 3 and 0.16 wt% of the total phases on day 5. The slag phase could form a melt and cause defluidisation in the bed, however the level of slag phase formed is likely too low to cause this. No defluidisation or operation difficulties were observed during operation although some melt formations were observed in the SEM micrographs on the particles.

The following figures summarize the phases which the trace elements Pb, Zn and Cu form in the gasifier and combustor for the investigated experimental days. Fig. 6 presents the phases which Pb forms at equilibrium in the gasifier and combustor respectively. A major part of Pb is present in the gas phase as  $PbCl_2$  in the gasifier. For day 2, 3, 5 and 13 mainly  $PbCl_2$  with minor amount of  $PbO$  and  $PbCl$  are transferred with the raw gas to the combustor where some of it is oxidized to  $PbO$  and  $Pb_2O_3$ . For day 1 and 5 where it is transferred with the solids from the gasifier, a slag phase is formed in the combustor. The formation of a slag phase observed in the following figures could possibly be explained by the addition of potassium on day 1 and 4 which increased the amount of slag phase, allowing dissolution of  $PbO$ .

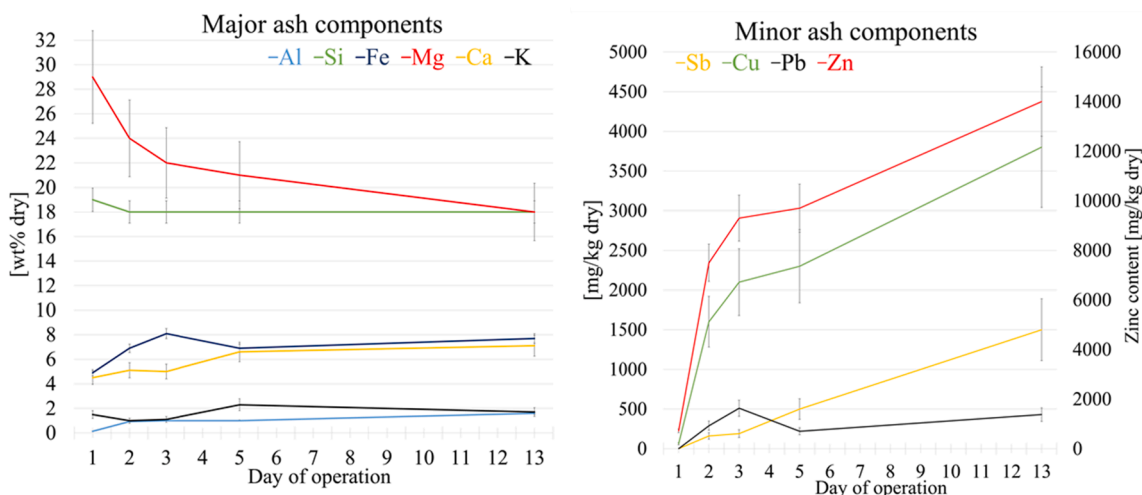


Fig. 3. The elemental composition in loop seals for day 1–3, 5 and 13. Major components are presented in the left figure. Minor ash components presented in the right figure with Zn-content on secondary y-axis. Error bars indicate measurement uncertainty.

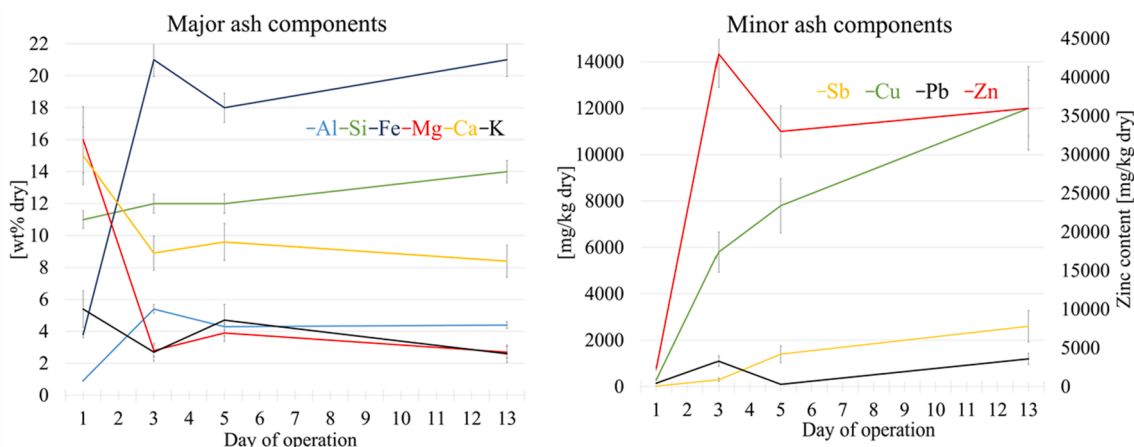


Fig. 4. Change in elemental composition in samples obtained from the secondary cyclone for day 1, 3, 5 and 13. Major components presented in the left figure. Minor ash components presented in the right figure with Zn-content on secondary y-axis. Error bars indicate measurement uncertainty.

Fig. 7 summarizes the phases which zinc forms in the gasifier and combustor respectively. In both cases, Zn is dissolved in a spinel phase,  $\text{ZnFe}_2\text{O}_4$  with the rest being combined with olivine,  $\text{MgZnSiO}_4$ . As seen from the figures a negligible amount of gaseous species is formed, but the main component of this stream is  $\text{ZnCl}_2$  and increases slightly with each calculation.

Fig. 8 below summarizes the phases which copper forms in the gasifier and combustor. There is a clear trend in the gasifier where copper ferrite is the most favorable compound. As the bed enters the combustor it is oxidized. In both the gasifier and the combustor, a small amount of gas is formed with the main gaseous component being copper chloride. For day 1 and 5 a major part of Cu is dissolved in a slag phase as  $\text{Cu}_2\text{O}$ .

### 3.1.2. Effect of reduction potential

Fig. 9 shows the molar phase distribution of Cu, Pb and Zn with increasing reduction potential. It is evident that both copper and zinc are kept solid with increasing reduction potential. Copper is retained either as copper ferrite under more oxidizing conditions between the reduction potentials  $-8.3$  and  $-5.3$ , or as copper sulfide either solid or solved in a slag phase under highly reducing conditions, between reduction potentials  $-3.8$  and  $-0.8$ . Zinc shows similar behavior to copper where it is kept solid throughout the reduction. Spinel,  $\text{ZnFe}_2\text{O}_4$  is the major constituent throughout reduction potentials  $-8.3$  and  $-3.8$  whereas olivine,  $\text{MgZnSiO}_4$ , and melilite,  $\text{Ca}_2\text{ZnSi}_2\text{O}_7$ , are formed above  $-3.8$ .

Lead is predominantly in the gas phase until reaching highly reducing conditions, the reduction potential  $-2.3$ . The gas phase consists of mainly  $\text{PbCl}_2$  in oxidizing environments with some  $\text{PbCl}$  forming for the moderately reducing environment. Highly reducing conditions, reduction potentials  $-2.3$  to  $-0.8$  favor formation of  $\text{Pb}$  (g) and  $\text{PbS}$  (g). However, a major part of lead is retained in the solid ashes as melilite, mainly as  $\text{Pb}_2\text{MgSi}_2\text{O}_7$ , and with further reduction in a slag phase as  $\text{PbS}$ . For the highest reduction potential, the total amount of slag phase only occupies 0.8 wt% of the total phases.

### 3.2. Ash characterization

The crystalline phases in the ash samples were investigated using XRD. The major crystalline phases were determined to be olivine ( $\text{Mg, Fe}_2\text{SiO}_4$ ), melilite ( $(\text{Na,Ca})_2\text{MgSi}_2\text{O}_7$ ), clinopyroxene ( $(\text{Ca,Mg,Fe,Al,Si})_3\text{SiO}_6$ ), spinel ( $(\text{Mg,Al,Zn,Fe})\text{Fe}_2\text{O}_4$ ) and feldspar ( $(\text{Na,K})\text{AlSi}_3\text{O}_8$ ) in all bottom ash samples (BA, LP1 and LP2). These phases are in line with the thermodynamic calculations presented in Fig. 5. The phase composition did not differ significantly between the ash samples, this is expected but also predicted in the thermodynamic calculations. The crystalline type

of compounds in the fly ash were identified to be sulfates ( $(\text{Na,K})_2\text{SO}_4$ ), hematite  $\text{Fe}_2\text{O}_3$  and chlorides ( $(\text{K,Na})\text{Cl}$ ) but contained also some of the crystalline phases found in the bottom ashes spinel ( $(\text{Mg,Al,Zn,Fe})\text{Fe}_2\text{O}_4$ ), clinopyroxene ( $(\text{Ca,Mg,Fe,Al,Si})_3\text{SiO}_6$ ) and feldspar ( $(\text{Na,K})\text{AlSi}_3\text{O}_8$ ).

In order to understand the interaction between the bed and ashes, morphology and chemical composition was further investigated using SEM-EDX. Mappings were performed to investigate the trends of zinc and copper. Lead and antimony however, are present at levels which are undetectable with the electron microscope. Point analyses were performed to investigate the composition in these Zn and Cu rich areas. Results are presented below for different ash fractions.

Fig. 10 shows the surface features of a bottom ash particle along with point analyses indicated in the figure. Point 1 and 2 contain higher amounts of Zn and Cu respectively, while point 3 shows the surface of the particle with no elevated intensities observed for either Cu or Zn. This figure shows spots with higher Fe-intensities. These originate from the ASR fuel ashes. Thus, an iron layer can be expected to form both from migration of Fe inside the olivine particle [42] but also from iron from the fuel ashes.

To investigate the presence of Cu and Zn in more detail, several mappings and point analyses were performed. Fig. 11 shows the cross section of a bottom ash particle and the ash layer. The formation of a Ca layer, previously described in olivine compounds, can be observed in the elemental mapping [20]. Fe may also be observed inside the particle, but with higher intensity at the surface. The migration of iron has been studied previously along with its oxygen carrying capabilities in olivine [42]. The intensity of Zn and Cu seems to be increased in the particle surface layer. Fig. S2 in Supplementary Material shows two bottom ash particles with a crack along with enrichment of Na and overlapping of K and S on the outermost surface.

Fig. 12 shows a cracked particle obtained from loop seal 1 along with elemental mapping. The micrograph of the whole particle is presented in Fig. S3 in Supplementary Material. A calcium layer can be observed on the surface of the particle along with Si, Fe and Mg. Zn is also observed both at the surface layer and inside the particle. Cu is unevenly distributed along with higher concentrations of Fe. Several point analyses were performed to investigate the concentration of the major and minor ash components. The results are presented in Fig. 12 along with the positions indicated in the figure. Point 1 and 3 were chosen to investigate the areas with higher intensities for Zn, while point 2 is chosen due to the high Cu-content. Point 4 serves as a reference where the intensity of both Cu and Zn are low. The point analysis shows that Zn is observed in points 1–3. At positions where the Fe-availability is higher a spinel phase is likely favored,  $\text{ZnFe}_2\text{O}_4$ .

Point analyses of particles obtained from loop seal 2 shows

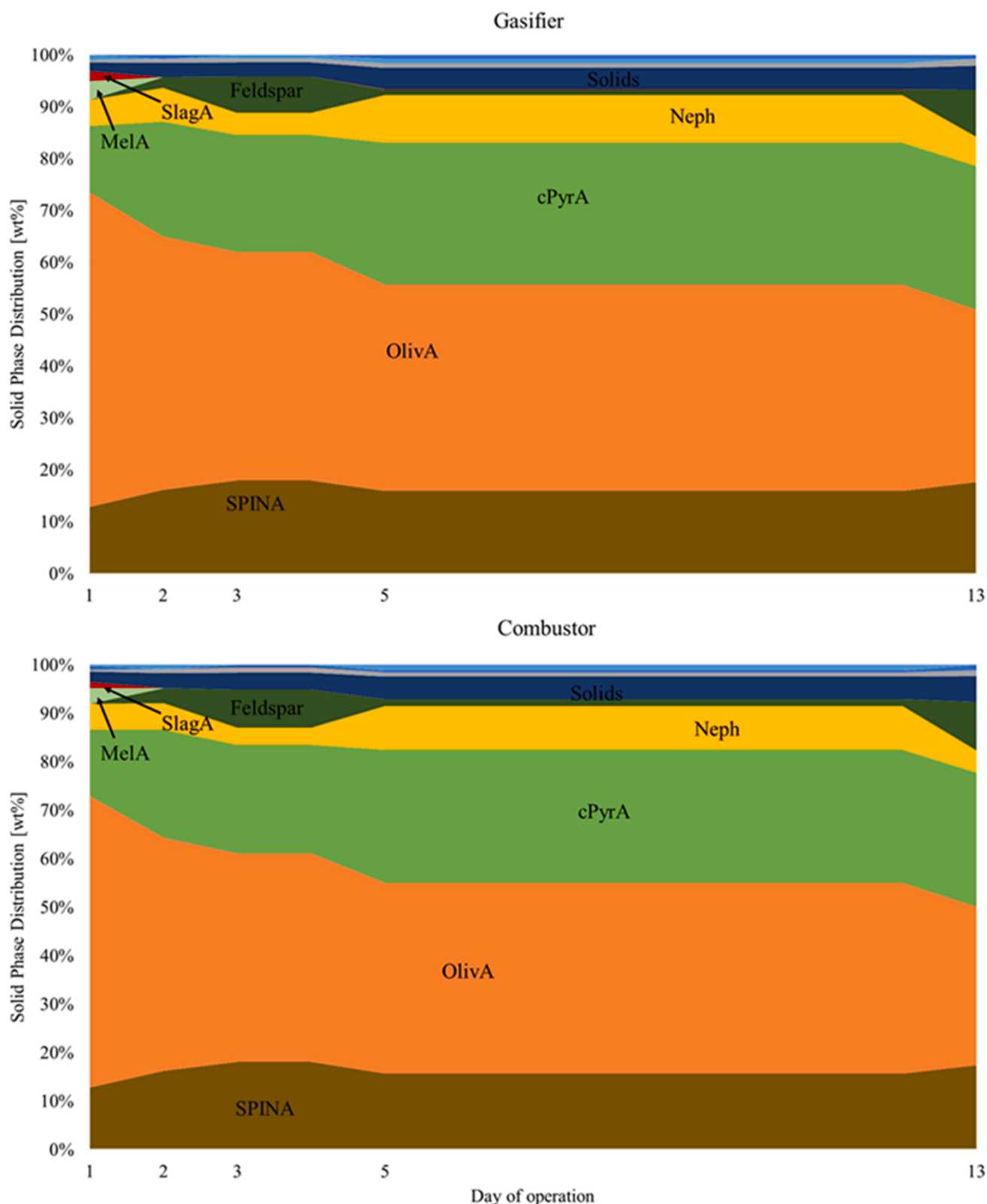


Fig. 5. Solid phase distribution predicted in the gasifier at 830 °C and oxygen partial pressure 10<sup>-5</sup> atm (upper figure) and combustor at 870 °C and oxygen partial pressure 0.05 atm (lower figure).

enrichment of Cu along with Fe in distinctive points. Point 1 in Fig. 13 shows one of these point analyses. Zinc showed low intensities in the mappings with some correlation with iron. The second point analysis shows the presence of zinc at the particle surface.

Fig. 14 shows fine particles in the fly ash along with larger pieces. An

overall image is presented in Fig. S4 in Supplementary Material. The submicron particles are enriched in Ca, K, Na, Cl and S while the larger particles contain more Fe and Si. Higher intensities of Cu can be observed at the larger particle surfaces. Point analysis at the surface of the larger particle shows higher content of Cu along with high content of

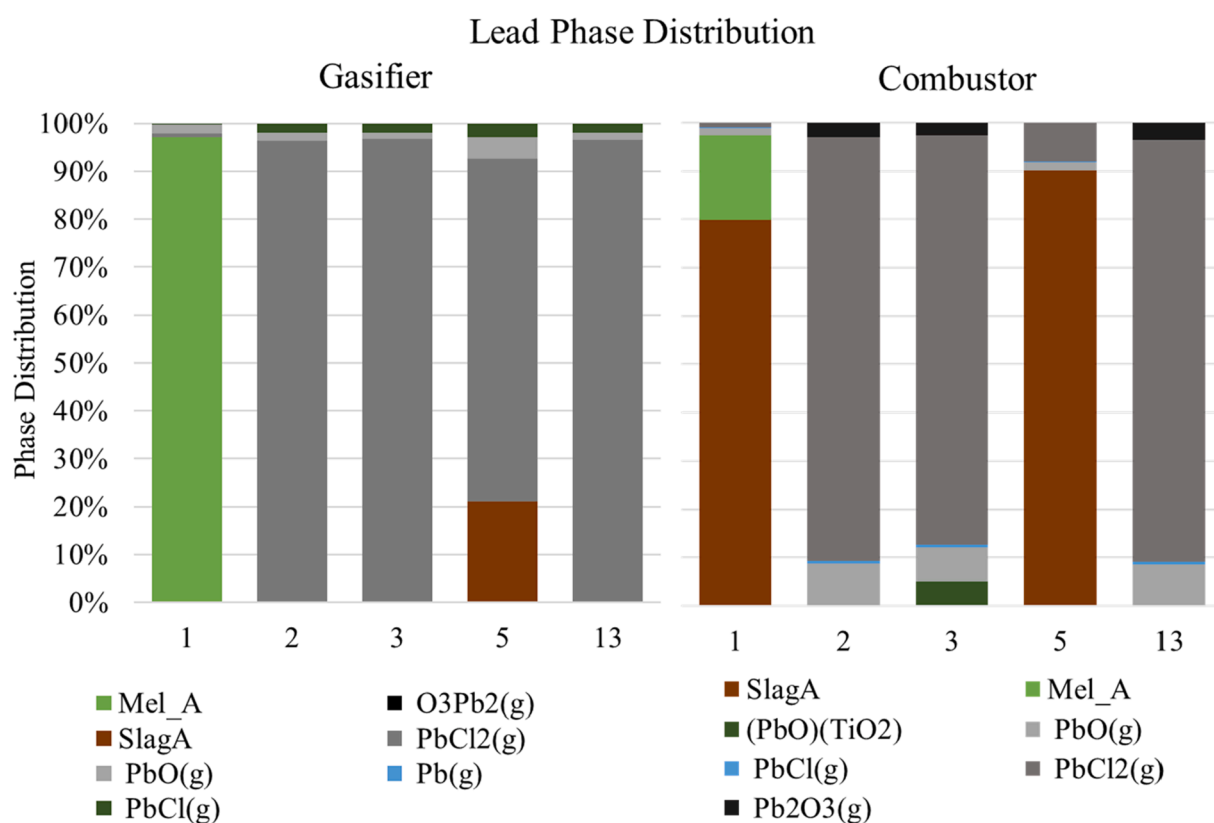


Fig. 6. Predicted phase distribution of lead in the gasifier at 830 °C and oxygen partial pressure  $10^{-5}$  atm (left figure) and combustor at 870 °C and oxygen partial pressure 0.05 atm (right figure).

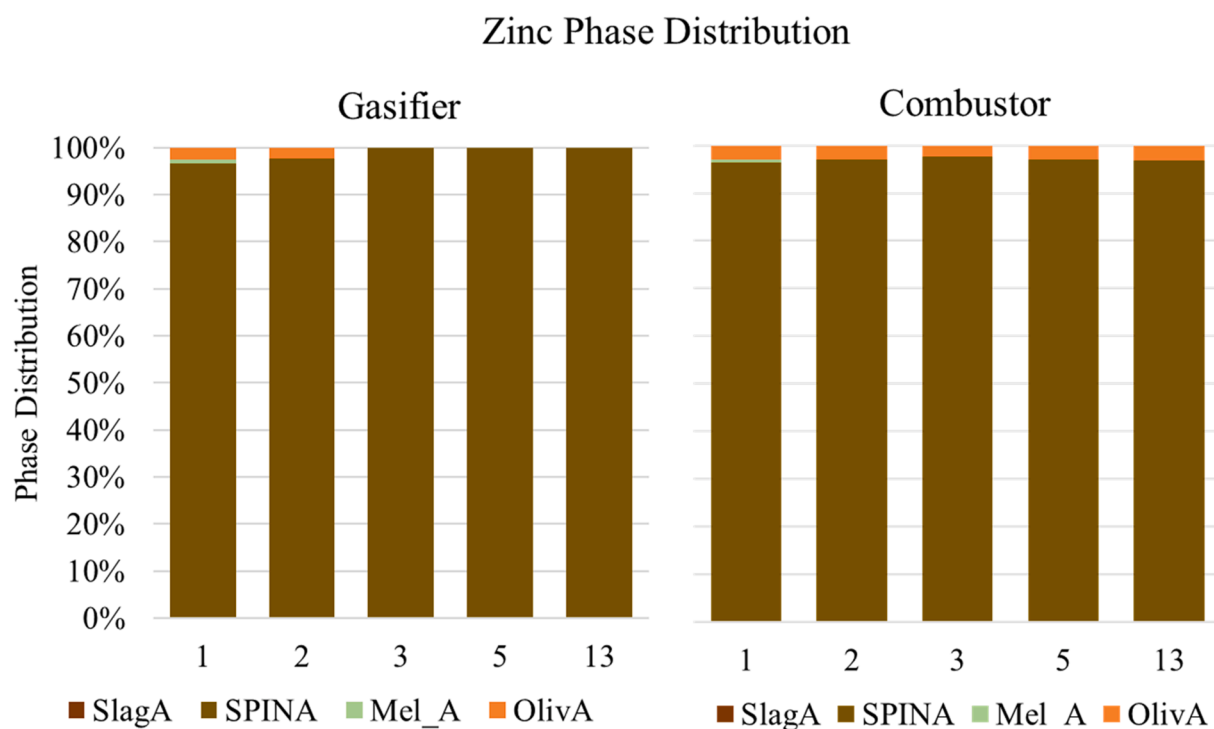
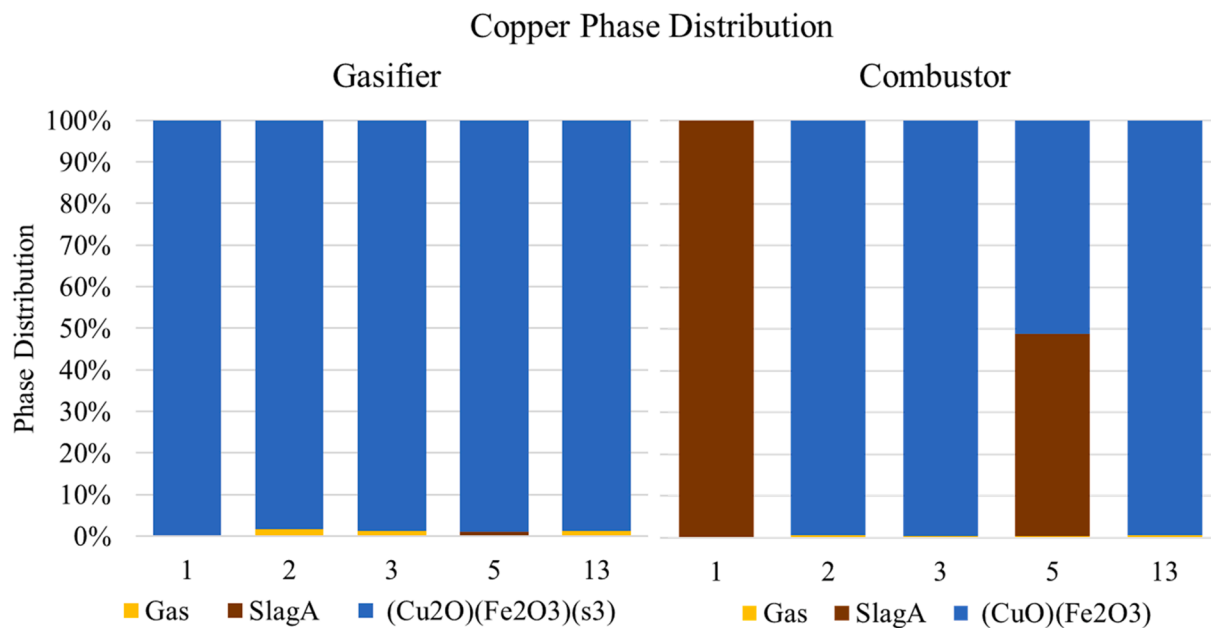
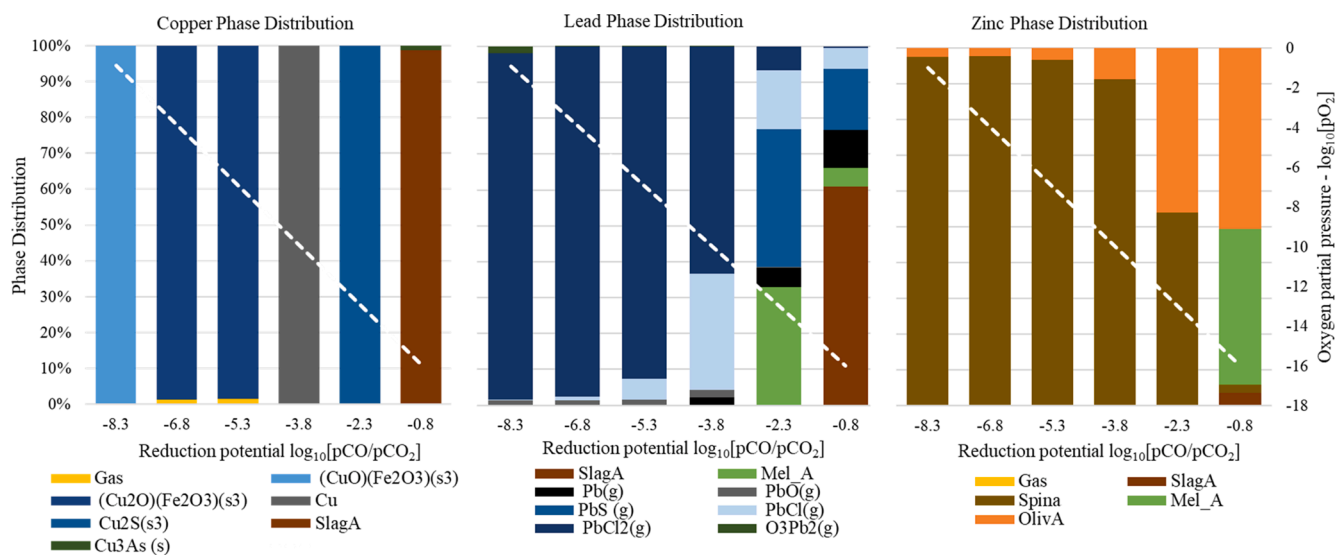


Fig. 7. Predicted phase distribution of zinc in the gasifier at 830 °C and oxygen partial pressure  $10^{-5}$  atm (left figure) and combustor at 870 °C and oxygen partial pressure 0.05 atm (right figure).



**Fig. 8.** Predicted phase distribution of copper in the gasifier at 830 °C and oxygen partial pressure  $10^{-5}$  atm (left figure) and combustor 870 °C and oxygen partial pressure 0.05 atm (right figure).



**Fig. 9.** Phase distribution of copper, lead and zinc with increasing reduction potential. Primary y-axis shows the phase distribution and secondary y-axis relates to the oxygen partial pressure, displayed for each element as a dashed white line.

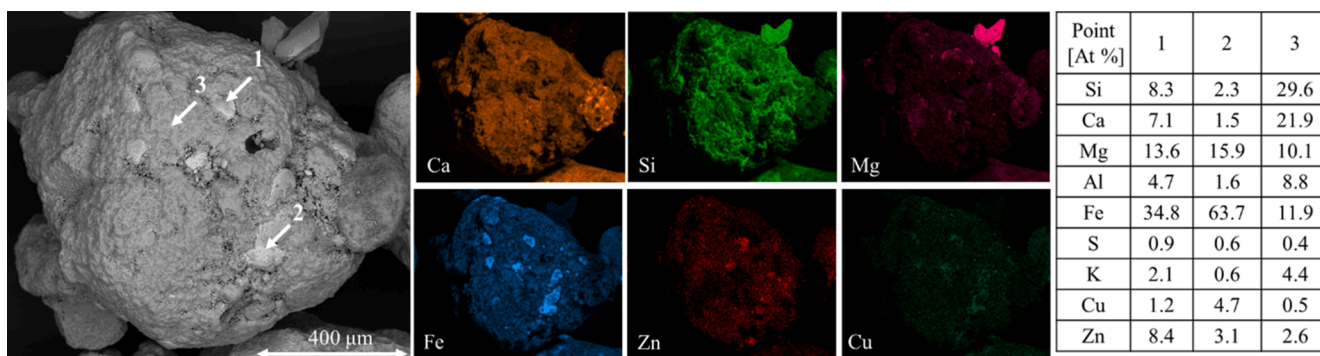


**Fig. 10.** Elemental mapping of the surface of a particle in the bottom ash (BA) from day 13, along with point analyses for the indicated areas.



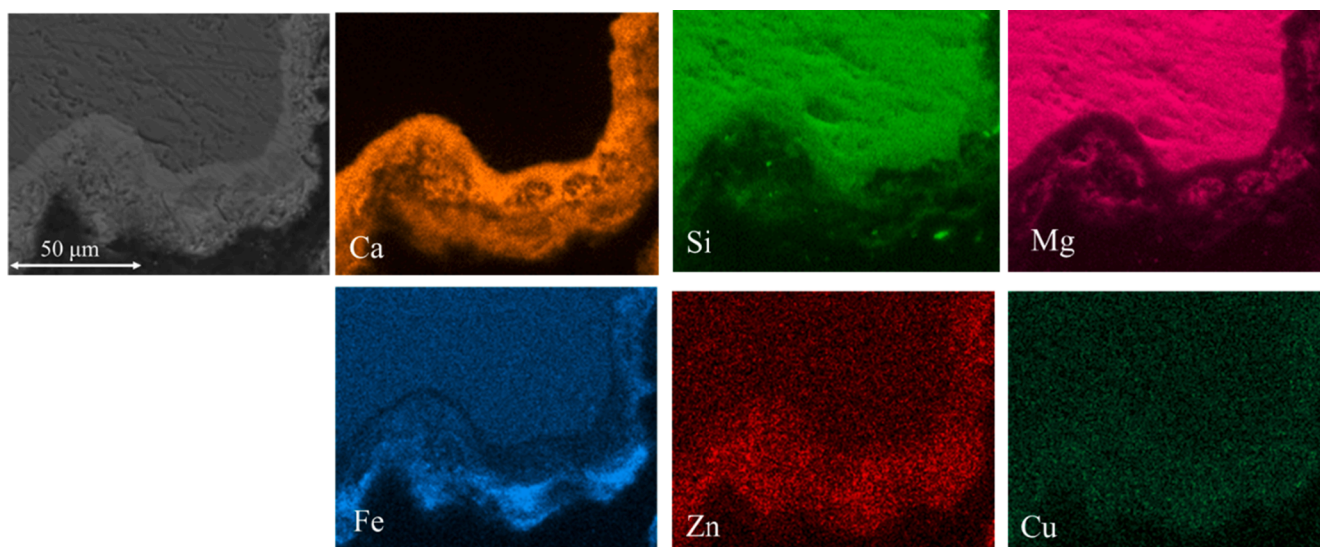


Fig. 11. Cross section of particle obtained from the bottom ash (BA) from day 13 along with mapping of the major elements along with Zn and Cu.

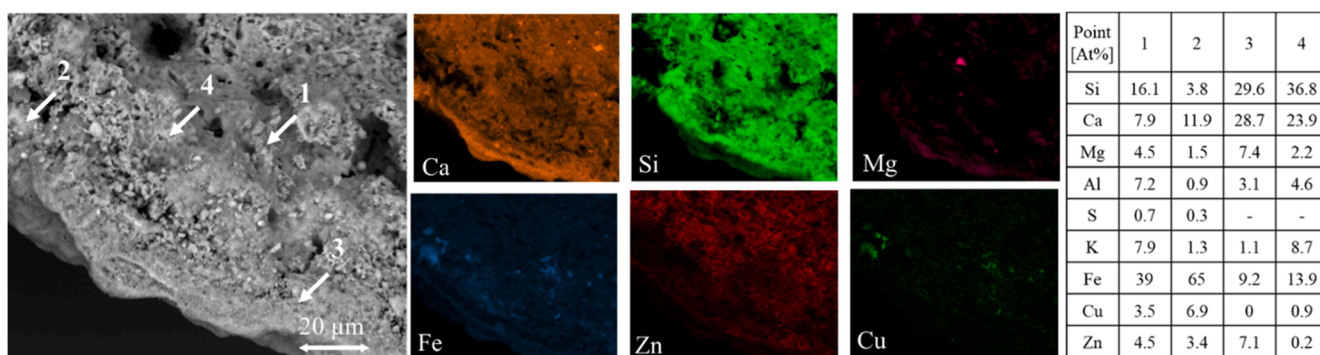


Fig. 12. Mapping of a particle, exposing its porous interior, obtained from loop seal 1 (LP1) on day 13. Points in figure indicate location for point analyses.

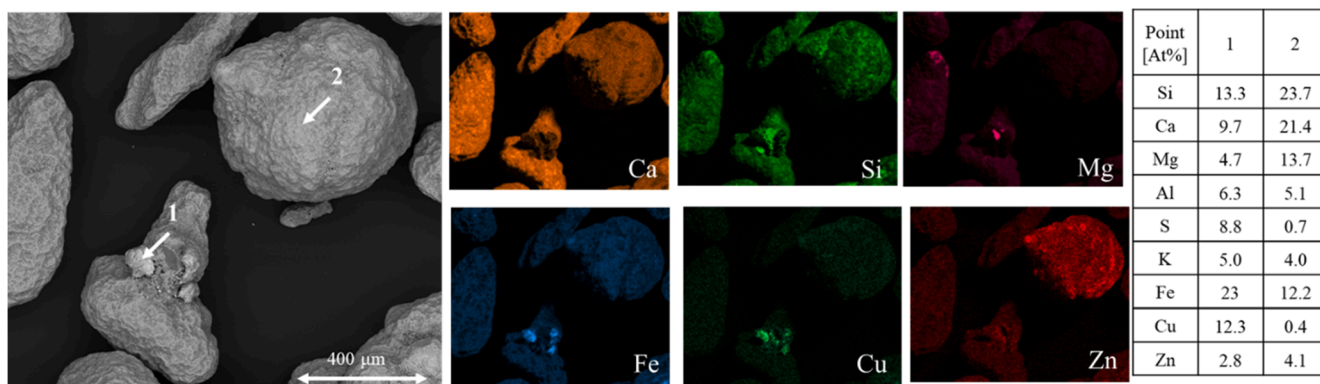


Fig. 13. Mapping of particles obtained from loop seal 2 (LP2) on day 13. Points in figure indicate location for point analyses.

Fe.

The results for different ash fractions have been presented in this section. The main crystalline phases and morphology in the bottom ash, LP1 and LP2 are shown to be very similar. The ash layer observed on the particle surface consists of iron, calcium, sodium and some aluminum. Zinc and copper were observed in distinctive points along with higher intensities of iron. Some cracked particles are observed in Figs. 11 and 12 which contribute to one part of the observed Zn and Cu in the fly ashes in Fig. 14.

### 3.2.1. Chemical speciation

Previous sections showed the presence of both Zn and Cu at the particle surfaces. However, the chemical states of these elements and the presence of Sb and Pb are still unknown. Therefore, the composition of the outermost surface is further investigated using XPS. The surface concentration of the reference and other ash fractions are presented in Table 5 using acronyms listed in Table 4. Point analyses on the fresh particles, as provided by supplier, is used as reference. The surface composition of the reference material is presented as a mean value based

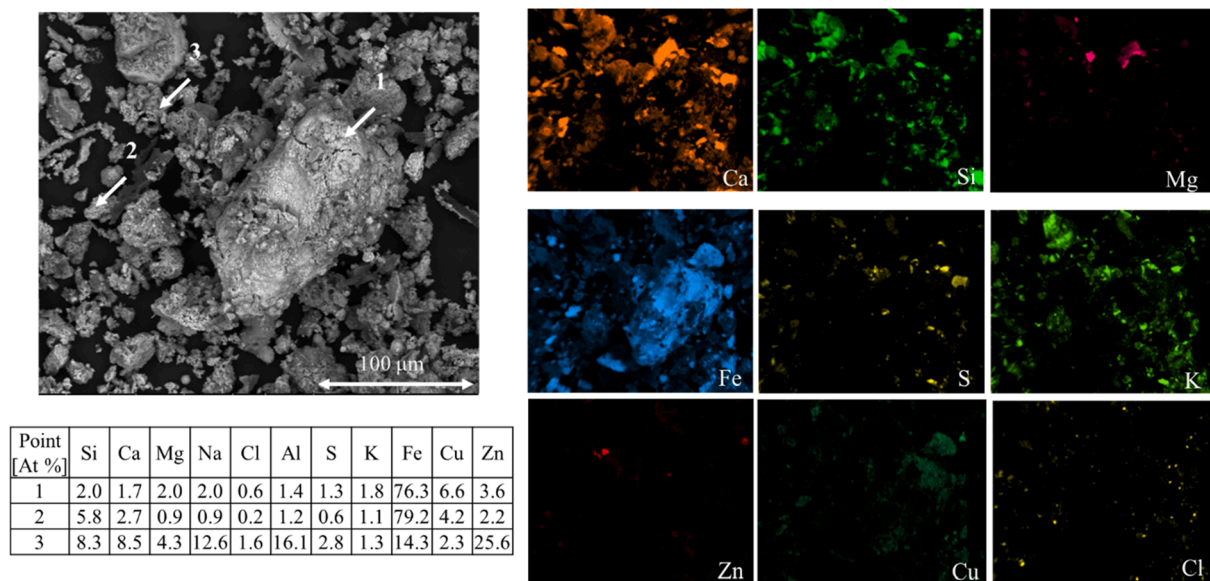


Fig. 14. Mapping of the fly ash (SC) sample along with point analyses in the indicated areas.

Table 5

Elemental composition (at%) at the particle surface obtained from the XPS-analysis for bottom ash (BA), loop seals (LP1 and LP2) and the fly ash from secondary cyclone (SC). Quantification performed using the peaks listed. Elements noted as < 0.1% indicates a small peak identified in the sample.

Sample [At%]	Peak	REF	1-BA	2-BA	3-BA	4-LP1	5-LP1	6-LP2	7-SC	8-SC
Mg	2s	42.5 ± 2.0	6.5	3.4	7.2	6.2	3.1	4.9	14.4	12.5
Si	2p	28.1 ± 0.7	10.3	2.9	7.1	6.1	6.0	6.6	5.0	5.3
Ca	2p	20.6 ± 0.6	7.4	6.6	10.6	12.4	8.6	6.9	5.0	4.4
Fe	2p	4.1 ± 0.3	1.8	1.5	3.4	2.0	5.6	3.0	5.6	5.4
Al	2p	3.1 ± 0.5	5.0	4.5	1.2	1.3	2.2	4.6	2.1	3.6
P	2p	0	0.7	0.2	0.8	1.0	0.7	1.8	1.8	0
S	2p	0	1.2	9.7	1.1	1.8	1.1	1.8	1.2	2.0
Cl	2p	0	0.2	0.8	0.3	0.5	0.2	0.7	1.5	1.2
K	2p	0	1.7	9.5	0.3	0	0.7	0.7	0.9	0.7
Na	1s	1.7 ± 1.1	2.8	1.3	2.8	2.8	4.3	5.1	2.3	3.7
Ti	2p	0	0	0	0.7	0	0	0.9	0	0
Mn	2p	0	1.0	0	0.5	0	0.8	0.9	0.8	0
Ba	3d <sub>5/2</sub>	0	0	0	0.1	0.2	0.3	0.3	1.8	0.7
Cu	2p <sub>3/2</sub>	0	1.7	1.5	0	0.2	0.6	1.8	1.8	1.0
Zn	2p <sub>3/2</sub>	0	0	0	0.6	0.3	1.0	0.6	0.6	1.0
Pb	4f	0	0	<0.1	0	<0.1	<0.1	0.1	0.2	0.2
Sb	3d <sub>3/2</sub>	0	0	0	1.0	0.7	0.4	0.4	<0.1	0.0

on three measurements.

The aim is to study the trends and behavior of these elements in the different fractions. By comparing the reference point in Table 5 with the samples from the bottom ash and loop seals an increase of Fe and Ca may be observed at the surface as well as a decrease of Si and Mg. Some amounts of Cu, Zn, Pb and Sb could be observed in both the fly ash and bed material. The chemical speciation of these elements was therefore

included in the following analysis.

High-resolution analyses were performed using low pass energy (26 eV) and narrow regions, unique for each element. The spectral regions Cu 2p, Pb 4f, Zn 2p and Sb 3d were selected in order to obtain more detailed information regarding their chemical states. The spectra were fitted using Multipak software and Shirley background, except for the case with Zn 2p where the smart background was used due to

Table 6

Summary of possible chemical states in each sample based on the XPS-analysis.

	2-BA	3-BA	4-LP1	6-LP2	7- SC
Copper	40.9% CuFe <sub>2</sub> O <sub>4</sub>	–	CuFe <sub>2</sub> O <sub>4</sub>	58.6% CuFe <sub>2</sub> O <sub>4</sub>	66.4% CuFe <sub>2</sub> O <sub>4</sub>
Zinc	59.1% CuSO <sub>4</sub>	–	ZnFe <sub>2</sub> O <sub>4</sub>	41.4% CuSO <sub>4</sub> ZnAl <sub>2</sub> O <sub>4</sub>	36.5% CuCl <sub>2</sub> 69.7% ZnFe <sub>2</sub> O <sub>4</sub>
Lead	–	–	–	PbSiO <sub>3</sub>	30.3% 56.7% ZnCl <sub>2</sub> PbO
Antimony	–	Sb <sub>2</sub> O <sub>3</sub>	Sb <sub>2</sub> O <sub>3</sub>	Sb <sub>2</sub> O <sub>5</sub> /SbFeO <sub>4</sub>	43.3% PbCl <sub>2</sub> Sb <sub>2</sub> O <sub>3</sub>

multileveled data. The fitted components are presented in Fig. S5 in Supplementary Material. The observed chemical states are discussed below and summarized in Table 6.

Cu 2p-spectrum was fitted using two components with parameters based on literature data. The two peaks which are used in the fitting procedure are located at  $932.9 \pm 0.1$  eV and  $935.0 \pm 0.2$  eV. The main peak  $932.9 \pm 0.1$  eV is accompanied by a satellite feature located at 942.8 eV which is in line with previous observations for  $\text{CuFe}_2\text{O}_4$  compounds [43,44]. The second peak was located at  $935.0 \pm 0.2$  eV for BA and LP2 and can be used to describe  $\text{CuSO}_4$ . The second peak for the SC-sample was located at 934.9 eV which can describe  $\text{CuCl}_2$  [38,45,46].

The Zn 2p-spectrum was fitted using one component except for SC where the peak was broader. The mean value of the main peaks for LP1, SC and BA are  $1021.0 \pm 0.1$  eV, corresponding to the reported value of  $\text{ZnFe}_2\text{O}_4$  [47]. The main peak for LP2 is located at 1022.2 eV, the region for  $\text{Zn}^{2+}$ -compounds, one of which  $\text{ZnAl}_2\text{O}_4$  has been reported in this region [48]. The second peak for SC is located at 1023.1 eV and ascribed to  $\text{ZnCl}_2$  [38,49].

The Pb 4f-spectrum was fitted using one component for LP2 and two components for SC. The main peak in LP2 is located at 138.8 eV which is in the range for  $\text{Pb}^{2+}$ . Compounds such as  $\text{PbSiO}_3$  and other forms of lead silicates have been described in this region [38,50]. Two peaks were used to fit the peak for SC. The first one is located at 138.4 eV, which is closest to the reported value of  $\text{PbO}$  [51]. The second peak is located at 139.3 eV and in the range of  $\text{PbCl}_2$  [50].

The whole Sb 3d-spectrum, between 525 eV and 545 eV, was collected for the fitting procedure. However, only the fitting for Sb  $3d_{3/2}$  is presented in Fig. S5 in Supplementary Material due to the overlapping of O 1s and Sb  $3d_{5/2}$ . The intensity and position of Sb  $3d_{5/2}$  were determined based on spin orbit splitting and ratio, in order to compare with literature. It is known from literature that it can be difficult to

distinguish between  $\text{Sb}^{3+}$  and  $\text{Sb}^{5+}$  oxidation states as the binding energy differs only by  $\sim 0.3$  eV [52]. It is also debated in the literature whether the oxidation state of Sb at the surface exist solely as  $\text{Sb}^{5+}$  [53] or as mixed  $\text{Sb}^{5+}/\text{Sb}^{3+}$  [54,55]. The data reported here cannot conclusively distinguish between these two. Nevertheless, a comparison with data reported in literature and different possibilities will be discussed. The Sb  $3d_{3/2}$  peak is located at  $539.5 \text{ eV} \pm 0.1$  eV (Sb  $3d_{5/2}$  peak at  $530.1 \pm 0.1$  eV) for the samples LP1 and BA. The Sb  $3d_{3/2}$  peak for SC is located at 539.2 eV (Sb  $3d_{5/2}$  peak at 529.8 eV). According to literature, these values are close to the reported value of  $\text{Sb}_2\text{O}_3$  and  $\text{Sb}_2\text{O}_4$  (Literature reports Sb  $3d_{5/2}$  peak to be located at  $530.2 \text{ eV} \pm 0.1$  eV for  $\text{Sb}_2\text{O}_3$ ,  $530.6 \text{ eV} \pm 0.1$  eV for  $\text{Sb}_2\text{O}_4$  and  $531.1 \text{ eV} \pm 0.1$  eV for  $\text{Sb}_2\text{O}_5$ ) [38,56]. The Sb  $3d_{3/2}$  peak for LP2 is located at 540.3 eV (Sb  $3d_{5/2}$  peak at 530.9 eV) in the range of the reported value for  $\text{Sb}_2\text{O}_5$  [56,57]. Another possibility is the formation of antimony ferrites. Studies have reported Sb  $3d_{3/2}$  peak to be located at 540.4 eV for the mixed oxide  $\text{SbFeO}_4$  which could be relevant for the LP2 sample [58,59].

### 3.2.2. Local thermodynamic calculations

Local thermodynamic calculations were performed using the detailed chemical composition obtained from the XPS-analysis presented in Table 5. The calculations were performed using the temperatures 870 °C for the bottom ash, 830 °C for the loop seals and 250 °C for the fly ash. The partial pressure of oxygen was set to 0.05 atm for both the bottom and fly ash while  $10^{-5}$  atm was used for the loop seals. The final calculations for the local equilibrium calculations consisted of 1341 species in total, 109 solutions and 459 phases. A summary of formed phases is presented in Table 7.

The local thermodynamic calculations predict the formation of copper and zinc ferrites in the bottom and fly ash, see Table 6 for comparison with experimental results. Copper is not included in the spinel solution and therefore predicted as a solid compound. A smaller

**Table 7**

Summary of formed phases in each sample for the elements Cu, Pb, Zn and Sb obtained from local thermodynamic calculations.

Sample	T [°C]	p(O <sub>2</sub> ) [atm]	Cu		Zn		Pb		Sb
1-BA	870	0.05	89.0%	$\text{Cu}_2\text{Fe}_2\text{O}_4$ (s)					
			6.4%	$\text{Cu}_2\text{O}$ SlagA					
			4.6%	$(\text{CuCl})_3$ (g)					
2-BA			70.7%	$\text{Cu}_2\text{Fe}_2\text{O}_4$ (s)			82.9%	$\text{PbCl}_2$ (g)	
			29.3%	$(\text{CuCl})_3$ (g)			17.1%	$\text{Pb}_2\text{MgSi}_2\text{O}_7$ Mel_A	
3-BA					96.6%	$\text{Zn}(\text{Fe,Al,Mg})_2\text{O}_4$ SpinA			$\text{SbO}_2$ (s)
4-LP1	830	$10^{-5}$			2.0%	$\text{CaZnSiO}_4$ OlivA			
					1.4%	$\text{ZnO}$ MeOA			
			93.7%	$\text{Cu}_2\text{O}$ SlagA	85.7%	$\text{Zn}(\text{Fe,Al,Mg})_2\text{O}_4$ SpinA	85.9%	$\text{PbO}$ SlagA	$\text{SbO}_2$ (s)
5-LP1			6.3%	$(\text{CuCl})_3$ (g)	13.9%	$\text{ZnO}$ MeOA	14.1%	$\text{PbCl}_2$ (g)	
					0.3%	$\text{ZnO}$ SlagA			
			83.7%	$\text{Cu}_2(\text{Fe}_2\text{O}_4)$ (s)	99.9%	$\text{Zn}(\text{Fe,Al,Mg})_2\text{O}_4$ SpinA		$\text{PbO}$ SlagA	$\text{SbO}_2$ (s)
6-LP2			16.3%	$\text{Cu}_2\text{O}$ SlagA	0.1%	$\text{ZnO}$ SlagA			
			92.5%	$\text{Cu}_2\text{Fe}_2\text{O}_4$ (s)	92.6%	$\text{Zn}(\text{Fe,Al,Mg})_2\text{O}_4$ SpinA	45.2%	$\text{PbCl}_2$ (g)	$\text{SbO}_2$ (s)
7-SC	250	0.05	4.9%	$\text{Cu}_2\text{O}$ SlagA	3.7%	$\text{Ca}_2\text{ZnSi}_2\text{O}_7$ OlivA	34.0%	$\text{PbO}$ SlagA	
			2.6%	$(\text{CuCl})_3$ (g)	3.5%	$\text{CaZnSiO}_4$ MelA	20.8%	$\text{Pb}_2\text{MgSi}_2\text{O}_7$ Mel_A	
					0.2%	$\text{ZnO}$ SlagA			
8-SC				$\text{CuFe}_2\text{O}_4$ (s)	77.5%	$\text{Zn}(\text{Fe,Al,Mg})_2\text{O}_4$ SpinA		$\text{Pb}_3\text{O}_4$ (s)	$\text{Sb}_2\text{O}_5$ (s)
					22.2%	$\text{ZnO}$ MeOA			
				$\text{CuFe}_2\text{O}_4$ (s)	85.4%	$\text{Zn}(\text{Fe,Al,Mg})_2\text{O}_4$ SpinA		$\text{Pb}_3\text{O}_4$ (s)	
					14.4%	$\text{ZnO}$ MeOA			
					0.2%	$\text{CaZnSiO}_4$ OlivA			



portion is predicted in the slag phase in the bottom ashes. Experiments suggest formation of copper sulfate while the available solid solutions in FactSage does not allow copper to dissolve in any of the sulfate-rich solid solutions. The addition of potassium sulfate to the combustor could induce areas with higher  $\text{SO}_2$ -partial pressures. This will favor formation of  $\text{CuSO}_4$  in the combustor, which is observed experimentally in Table 6. A predominance plot of copper with  $\text{SO}_2$  and  $\text{O}_2$  showed that formation of  $\text{CuSO}_4$  is possible at  $870^\circ\text{C}$  with high  $\text{O}_2$  and  $\text{SO}_2$  partial pressures. With lower  $\text{O}_2$  partial pressures  $\text{Cu}_2\text{S}$  forms, which could occur in the gasifier locally. If  $\text{Cu}_2\text{S}$  forms it can oxidize to  $\text{CuSO}_4$  in the combustor, or after extraction during cooldown in air. Zinc is bound in a spinel phase with mainly Fe, but also some Mg and Al. The spinel observed in LP2 contained higher amount of  $\text{ZnAl}_2\text{O}_4$  compared to other fractions. As observed experimentally in Table 6 the major Zn-component is a spinel. In the fly ash, zinc and lead chlorides were also observed. This indicates that gaseous  $\text{ZnCl}_2$  and  $\text{PbCl}_2$  has formed in the process and condensed downstream. Lead is predominantly found in the slag phase as  $\text{PbO}$  but some  $\text{PbCl}_2$  is predicted in BA, LP1 and LP2.  $\text{PbCl}_2$  has a melting point of  $500^\circ\text{C}$ , which could condense on the particles or another possibility is that  $\text{PbCl}_2$  interacts with  $\text{SiO}_2$  to form lead silicates [60] which could be the case in LP2, see Table 6. However, the available thermodynamic data for lead silicate compounds is scarce and in need of further evaluation. In the fly ash lead is predicted as  $\text{Pb}_3\text{O}_4$ , which oxidizes from  $\text{PbO}$  at temperatures below  $420^\circ\text{C}$ . Antimony is predicted to form  $\text{SbO}_2$  (s) in every sample except in the fly ash where  $\text{Sb}_2\text{O}_5$  (s) is formed. The available data for solid Sb compounds includes mixed Sb-metal compounds but no mixed oxides. Hence the formation of antimony ferrites is impossible without expanding the database.

The local thermodynamic calculations show which compounds could be expected at the surface of the particles in contrast to the global calculations where the main phases in the reactors are presented. The local calculations predict the major phases at the surface to be olivine, spinel, melilite, clinopyroxene, sulfates ( $(\text{K},\text{Na})_2\text{SO}_4$  and small amount of slag. As these are related to the ASR-fuel and chemical additions it is not surprising to find these compounds at the surface of the particles. These compounds are also well aligned with the main phases predicted by the global equilibrium calculation in Fig. 5.

#### 4. Discussion

This paper has used several experimental methods and thermodynamics to analyse the chemical transformations that can occur during chemical looping gasification of ASR waste. More specifically the focus has been on the fate of the trace elements Zn, Cu, Pb and Sb. These elements can be prevalent in ASR waste, in some cases have economic value but also cause environmental issues in ash.

The combined results of thermodynamic equilibrium calculations and different ash characterization techniques show a complex picture where a number of transformations can occur. Fig. 15 illustrates a system of possible main reaction pathways according to experimental results and thermodynamic predictions in this paper. The figure shows reaction pathways from the metals in the fuel to formation of solid ash compounds and gaseous compounds such as  $\text{MCl}_2$ ,  $\text{MO}$ ,  $\text{M}$  and  $\text{M}_2\text{SO}_4$  where  $\text{M}$  stands for the metals  $\text{M} = \text{Zn}, \text{Cu}, \text{Pb}$  and  $\text{Sb}$ . The illustration shows complex chemistry which are related to the following:

- Competing balances between S and Cl in the system are known to alter the volatility behavior of metals where S may decrease the volatility due to formation of condensed sulfates and Cl may promote formation of gaseous metal chlorides [61].
- Volatilization behavior is further affected by the alkali in the system as the affinity towards alkali chlorides is higher compared to heavy metals [62,63].
- Volatilization of the heavy metals also depend on temperature, reduction potential and ash composition [64].

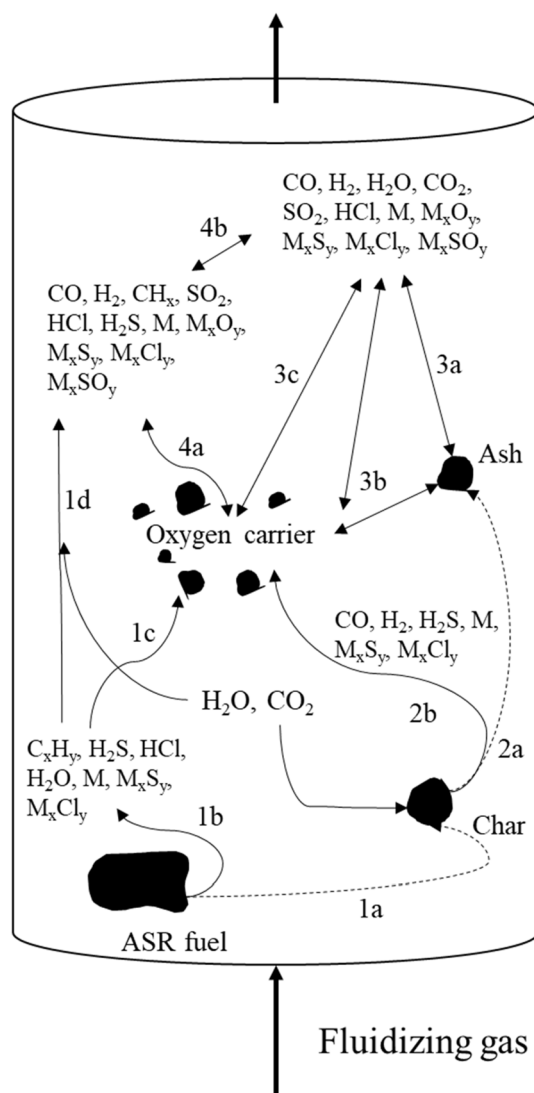


Fig. 15. A summary of possible pathways for the elements  $\text{M} = \text{Cu}, \text{Zn}, \text{Sb}$  and  $\text{Pb}$  compiled based on experimental results and thermodynamic equilibrium prediction as performed in this study.

- The bed material and ashes interact with alkali in the system changing the levels in the gaseous phase, which in its turn could affect the pathways of the heavy metals.
- The complex chemistry may also be related to the fuel particle size, structure and residence time.

The thermal conversion path of ASR can be observed in Fig. 15 with the drying and devolatilization stage (1a) and char burnout (2a). During devolatilization and drying, components such as  $\text{C}_x\text{H}_y$ ,  $\text{HCl}$ ,  $\text{H}_2\text{S}$ ,  $\text{H}_2\text{O}$  but also organically associated heavy metals ( $\text{M} = \text{Cu}, \text{Zn}, \text{Sb}$  and  $\text{Pb}$ ) are released (1b). The products can either interact directly with the bed material (1c) or in presence of the fluidization gas they oxidize and/or interact with each other to form new compounds (1d). Metals which are bound in complex chemical structures could be released at a later stage and interact with the bed material (2b) or be oxidized by the fluidization gas (following the 3c path). Formation of metal chlorides ( $\text{M}_x\text{Cl}_y$ ) may occur by both direct and indirect chlorination (1d, 4b) [62]. For indirect chlorination  $\text{HCl}$  and/or  $\text{Cl}_2$  are first formed by reaction with  $\text{H}_2\text{O}/\text{O}_2$ . Thereafter  $\text{HCl}/\text{Cl}_2$  may react with the metals or metal oxides to form metal chlorides. Direct chlorination occurs directly between chlorides ( $\text{NaCl}, \text{KCl}, \text{CaCl}_2, \text{MgCl}_2$  etc) in the gas phase and the metal oxide [62]. The formed metal chlorides may thereafter continue to interact with the

bed material (4a, 3c) or ash (3a) to form new solid and/or gaseous compounds. Furthermore, the formed gas components can react with both the ash and the bed material (3a-c and 4a). The total amount of metals released depends on several factors such as temperature, reduction potential but also the Cl- and S-chemistry. The main ash species, e.g.  $\text{Fe}_3\text{O}_4$ ,  $\text{Al}_2\text{O}_3$ ,  $\text{SiO}_2$  etc... may also interact with the bed material (3b) or metals in the gas phase (3a) to form new compounds. This study has found that the possible compound formation for the investigated metals Cu, Zn, Pb and Sb is mainly with iron, aluminum and silicone forming  $(\text{Zn,Cu,Sb})\text{Fe}_x\text{O}_y$ ,  $(\text{Zn,Cu,Pb})\text{Al}_x\text{O}_y$ ,  $(\text{Pb,Cu,Zn})_x\text{SiO}_y$  and  $(\text{Ca,Na,Pb})_2(\text{Zn,Mg,Fe,Al})\text{Si}_2\text{O}_7$  in the bottom ash or oxides and  $(\text{Zn,Cu,Pb})\text{Cl}_x$  in the gas phase which condensate and/or undergo sulfation and eventually end up in the fly ash. At lower temperatures sulfates become more stable than chlorides, especially if there is  $\text{SO}_2$  and oxygen available.

Experimental investigation was performed in this study to map the chemical interaction which occur with the bed material as discussed above. The chemical speciation of Cu, Sb, Pb and Zn were investigated in ash samples extracted on the last day of operation, day 13. Elemental mapping of particles, Figs. 11 and 12, show a Fe and Ca-layer, as described in literature [20,42]. Similar Fe-migration has been observed in cases using ilmenite as bed material [65]. Iron migrates to locations with higher oxygen partial pressure and in case of large pores or cracks the migration may be enhanced. Besides the migration, a large fraction of Fe is available in the ASR ashes which enhanced the formation of an iron layer. The interaction with ASR ash is evident in Fig. 10 where areas with higher iron concentration are observed in distinctive points. The presence of iron oxide at the surface opens up for the possibility of transferring oxygen to areas with lower partial pressures of oxygen in the reactor, for example into the gasifier, creating a chemical looping gasification process. Further, the presence of these Fe-islands also enables the bed material to interact with Cu, Zn and Sb to form ferrites. Figs. 3 and 4 shows that the content of Cu and Zn follow the same increasing trend as the content of Fe in both the loop seals and secondary cyclone. The SEM-micrographs confirm the coexistence of Fe and Cu and Zn on the surface of the particles, while the XPS-analysis suggests formation of copper, zinc and antimony ferrites on the outermost surface of the particles. In chemical looping systems where oxygen transport is wanted, such as CLG, Chemical Looping Combustion (CLC) or Oxygen Carrier Aided Combustion (OCAC) formation of copper and zinc ferrites would likely not hinder the release of oxygen in comparison to pure iron oxides as for example, copper ferrites [66–68] and zinc ferrites [69] have previously been studied as oxygen carriers [69]. Zinc also has a possibility to be incorporated into the olivine structure, which means that there are further interaction possibilities not only with the ash layer but also with the core of the particle. The main reaction path for solid Pb-compounds seems to be with silica. A major part of lead can be expected to enter the gas phase as  $\text{PbCl}_2$  and through the metal matrix reaction lead silicates could form [60]. If these heavy elements interact with the bed material to form stable compounds, such as ferrites and silicates, it may be beneficial from different perspectives:

- Release of heavy metals to the gas phase is hindered, which reduces the risk of fouling and corrosion but also heavy metal emission [70,71].
- The content of heavy metals in the fly ash could be lowered which decreases the toxicity and could eventually lower costs related to disposal [72].
- If heavy metals are bonded in a stable matrix in the bottom ash and not leached out during weather conditions disposal handling could be facilitated. Another possibility, by concentrating heavy metals in the bottom ash, is to investigate different leaching processes which could be utilized for metal extraction.
- Formation of certain compounds, for example copper aluminates, have low leachability and could hinder recovery [73]. The leachability of the compounds in oxygen carriers have not been studied in

this paper and thus the possibility, efficiency and optimal parameters need to be further investigated.

## 5. Conclusion

This study has investigated ash samples from a semi-commercial plant with a specific focus on the elements Cu, Pb, Zn and Sb. An experimental approach along with a thermodynamic evaluation of chemical looping gasification of ASR has been performed and the fate of these elements has been investigated. The study showed that iron has a significant effect on the trace element speciation, especially for Cu and Zn where ferrites are formed. The reduction potential affects the phase distribution of these elements where highly reduction conditions result in heavy metals dissolving in the slag phase. The crystalline phases predicted in the global thermodynamic calculations are well aligned with the phases obtained experimentally. However, the local thermodynamic calculations have identified that data for mixed antimony oxides and certain lead silicates are missing. The results in this study can have implications for ash characteristics and corrosion phenomena during chemical looping gasification.

## CRedit authorship contribution statement

**Ivana Staničić:** Writing - original draft, Methodology, Investigation, Formal analysis, Visualization. **Isabel Cañete Vela:** Resources, Conceptualization, Investigation, Writing - review & editing. **Rainer Backman:** Supervision, Writing - review & editing, Validation. **Jelena Maric:** Resources, Conceptualization, Investigation, Writing - review & editing. **Yu Cao:** Supervision, Writing - review & editing, Validation. **Tobias Mattisson:** Supervision, Methodology, Conceptualization, Writing - review & editing.

## Declaration of Competing Interest

The authors declare that they have no known competing financial interests or personal relationships that could have appeared to influence the work reported in this paper.

## Acknowledgements

This work was financed by Formas, the Swedish Research Council for Environment, Agricultural Sciences and Spatial Planning (2017-01095), STEM-CLG, The Swedish Energy Agency (43220-1, 44239-1) and the Swedish Gasification Center (SFC). This work was performed in part at the Chalmers Material Analysis Laboratory, CMAL. The authors acknowledge the valuable assistance provided by research engineers Jessica Bohwalli, Johannes Öhlin and Rustan Marberg.

## Appendix A. Supplementary data

Supplementary data to this article can be found online at <https://doi.org/10.1016/j.fuel.2021.121147>.

## References

- [1] ACEA Report: Vehicles in use Europe 2019. European Automobile Manufacturers Association; 2019.
- [2] Cossu R, Lai T. Automotive shredder residue (ASR) management: an overview. *Waste Manage* 2015;45:143–51.
- [3] Directive 2000/53/EC of the European Parliament and the Council of 18 September 2000 on end-of-life vehicles, OJ L 269, 21.10.2000.
- [4] European Commission. Communication from the commission to the European parliament, the council, the European economic and social committee and the committee of the region - The role of waste-to-energy in the circular economy. Brussels 2017.
- [5] Wilk V, Hofbauer H. Conversion of mixed plastic wastes in a dual fluidized bed steam gasifier. *Fuel* 2013;107:787–99.
- [6] Hanchate N, Ramani S, Mathpati CS, Dalvi VH. Biomass gasification using dual fluidized bed gasification systems: a review. *J Cleaner Prod* 2021;280:123148.

- [7] Thunman H, Seemann M, Berdugo Vilches T, Maric J, Pallares D, Ström H, et al. Advanced biofuel production via gasification – lessons learned from 200 man-years of research activity with Chalmers' research gasifier and the GoBiGas demonstration plant. *Energy Sci Eng* 2018;6:6–34.
- [8] Condori O, García-Labiano F, de Diego LF, Izquierdo MT, Abad A, Adánez J. Biomass chemical looping gasification for syngas production using ilmenite as oxygen carrier in a 1.5 kWth unit. *Chemical Engineering Journal*. 2021;405: 126679.
- [9] Hildor F, Leion H, Linderholm CJ, Mattisson T. Steel converter slag as an oxygen carrier for chemical-looping gasification. *Fuel Process Technol* 2020;210:106576.
- [10] Yu Z, Yang Y, Yang S, Zhang Q, Zhao J, Fang Y, et al. Iron-based oxygen carriers in chemical looping conversions: a review. *Carbon Resour Convers* 2019;2:23–34.
- [11] Ge H, Guo W, Shen L, Song T, Xiao J. Biomass gasification using chemical looping in a 25kWth reactor with natural hematite as oxygen carrier. *Chem Eng J* 2016; 286:174–83.
- [12] Larsson A, Seemann M, Neves D, Thunman H. Evaluation of performance of industrial-scale dual fluidized bed gasifiers using the chalmers 2–4-MWth gasifier. *Energy Fuels* 2013;27:6665–80.
- [13] Maric J, Berdugo Vilches T, Thunman H, Gyllenhammar M, Seemann M. Valorization of automobile shredder residue using indirect gasification. *Energy Fuels* 2018;32:12795–804.
- [14] Pissot S, Berdugo Vilches T, Maric J, Cañete Vela I, Thunman H, Seemann M. Thermochemical recycling of automotive shredder residue by chemical-looping gasification using the generated ash as oxygen carrier. *Energy Fuels* 2019;33: 11552–66.
- [15] Faust R, Berdugo Vilches T, Malmberg P, Seemann M, Knutsson P. Comparison of ash layer formation mechanisms on Si-containing bed material during dual fluidized bed gasification of woody biomass. *Energy Fuels* 2020;34:8340–52.
- [16] He H, Boström D, Öhman M. Time dependence of bed particle layer formation in fluidized quartz bed combustion of wood-derived fuels. *Energy Fuels* 2014;28: 3841–8.
- [17] Morris JD, Daoud SS, Nimmo W. Agglomeration and the effect of process conditions on fluidized bed combustion of biomasses with olivine and silica sand as bed materials: pilot-scale investigation. *Biomass Bioenergy* 2020;142:105806.
- [18] Grimm A, Öhman M, Lindberg T, Fredriksson A, Boström D. Bed agglomeration characteristics in fluidized-bed combustion of biomass fuels using olivine as bed material. *Energy Fuels* 2012;26:4550–9.
- [19] Kern S, Pfeifer C, Hofbauer H. Reactivity tests of the water–gas shift reaction on fresh and used fluidized bed materials from industrial DFB biomass gasifiers. *Biomass Bioenergy* 2013;55:227–33.
- [20] Kirnbauer F, Hofbauer H. The mechanism of bed material coating in dual fluidized bed biomass steam gasification plants and its impact on plant optimization. *Powder Technol* 2013;245:94–104.
- [21] Kuba M, He H, Kirnbauer F, Skoglund N, Boström D, Öhman M, et al. Mechanism of layer formation on olivine bed particles in industrial-scale dual fluid bed gasification of wood. *Energy Fuels* 2016;30:7410–8.
- [22] Morris JD, Daoud SS, Chilton S, Nimmo W. Mechanisms and mitigation of agglomeration during fluidized bed combustion of biomass: a review. *Fuel* 2018; 230:452–73.
- [23] Kirnbauer F, Hofbauer H. Investigations on bed material changes in a dual fluidized bed steam gasification plant in güssing, Austria. *Energy & Fuels* 2011;25:3793–8.
- [24] Faust R, Sattari M, Maric J, Seemann M, Knutsson P. Microscopic investigation of layer growth during olivine bed material aging during indirect gasification of biomass. *Fuel* 2020;266.
- [25] Devi L, Craje M, Thüne P, Ptasiński KJ, Janssen FJJG. Olivine as tar removal catalyst for biomass gasifiers: Catalyst characterization. *Appl Catal A* 2005;294: 68–79.
- [26] Virginie M, Adánez J, Courson C, de Diego LF, García-Labiano F, Niznansky D, et al. Effect of Fe–olivine on the tar content during biomass gasification in a dual fluidized bed. *Appl Catal B* 2012;121–122:214–22.
- [27] Gonzalez-Fernandez O, Hidalgo M, Margui E, Carvalho ML, Queralt I. Heavy metals' content of automotive shredder residues (ASR): Evaluation of environmental risk. *Environ Pollut* 2008;153:476–82.
- [28] Zevenhoven R, Saeed L. Automotive Shredder Residue (ASR) and Compact Disc (CD) Waste Options for Recovery of Materials and Energy. Espoo (Finland): Helsinki University of Technology; 2003.
- [29] Reed GP, Dugwell DR, Kandiyoti R. Control of trace elements in gasification: distribution to the output streams of a pilot scale gasifier. *Energy Fuels* 2001;15: 794–800.
- [30] Clarke LB. The fate of trace elements during coal combustion and gasification: an overview. *Fuel* 1993;72:731–6.
- [31] Elled AL, Amand LE, Leckner B, Andersson BÅ. The fate of trace elements in fluidised bed combustion of sewage sludge and wood. *Fuel* 2007;86:843–52.
- [32] Nzihou A, Stanmore B. The fate of heavy metals during combustion and gasification of contaminated biomass—A brief review. *J Hazard Mater* 2013; 256–257:56–66.
- [33] Salo K, Mojtahedi W. Fate of alkali and trace metals in biomass gasification. *Biomass Bioenergy* 1998;15:263–7.
- [34] Konttinen J, Backman R, Hupa M, Moilanen A, Kurkela E. Trace element behavior in the fluidized bed gasification of solid recovered fuels – A thermodynamic study. *Fuel* 2013;106:621–31.
- [35] Priscak J, Fürsatz K, Kuba M, Skoglund N, Benedikt F, Hofbauer H. Investigation of the formation of coherent ash residues during fluidized bed gasification of wheat straw lignin. *Energies* 2020;13(3935).
- [36] Naumkin VA, Kraut-Vass A, Gaarenstroom SW, Powell CJ. NIST X-ray Photoelectron Spectroscopy Database - NIST Standard Reference Database 20, Version 4. 6 June 2000 ed. Gaithersburg MD, 20899: National Institute of Standards and Technology; 2012.
- [37] Biesinger MC, Payne BP, Grosvenor AP, Lau LWM, Gerson AR, Smart RSC. Resolving surface chemical states in XPS analysis of first row transition metals, oxides and hydroxides: Cr, Mn, Fe, Co and Ni. *Applied Surface Science*. 2010;257: 2717–30.
- [38] Moulder JM, Stickle WF, Sobol PE, Bomben Kd. Handbook of X-ray Photoelectron Spectroscopy - A Reference Book of Standard Spectra for Identification and Interpretation of XPS Data. 6509 Flying Cloud Drive Eden Prairie, Minnesota 55344 United States of America: Perkin-Elmer Corporation - Physical Electronics Division; 1992.
- [39] Bale CW, Bélsile E, Chartrand P, Decterov SA, Eriksson G, Gheribi AE, et al. FactSage thermochemical software and databases - 2010–2016. *Calphad* 2016;54: 35–53.
- [40] Stanić I, Mattisson T, Backman R, Cao Y, Rydén M. Oxygen Carrier Aided Combustion (OCAC) of Two Waste Fuels Experimental and Theoretical Study of the Interaction between Ilmenite and Zinc, Copper and Lead. [Manuscript submitted for publication].
- [41] Roine A. HSC chemistry® [Software]. Pori: Outotec; 2018.
- [42] Lancee RJ, Dugulan AI, Thüne PC, Veringa HJ, Niemantsverdriet JW, Fredriksson HOA. Chemical looping capabilities of olivine, used as a catalyst in indirect biomass gasification. *Appl Catal B* 2014;145:216–22.
- [43] Li X, Liu A, Chu D, Zhang C, Du Y, Huang J, et al. High performance of manganese porphyrin sensitized p-type CuFe2O4 photocathode for solar water splitting to produce hydrogen in a tandem photoelectrochemical cell. *Catalysts* 2018;8:108.
- [44] McIntyre NS, Cook MG. X-ray photoelectron studies on some oxides and hydroxides of cobalt, nickel, and copper. *Anal Chem* 1975;47:2208–13.
- [45] Vasquez RP. CuCl2 by XPS. *Surf Sci Spectra* 1993;2:160–4.
- [46] Biesinger MC. Advanced analysis of copper X-ray photoelectron spectra. *Surf Interface Anal* 2017;49:1325–34.
- [47] Karamat S, Rawat RS, Lee P, Tan TL, Ramanujan RV. Structural, elemental, optical and magnetic study of Fe doped ZnO and impurity phase formation. *Prog Nat Sci Mater Int* 2014;24:142–9.
- [48] Iaiche S, Djelloul A. ZnO/ZnAl2O4 nanocomposite films studied by X-ray diffraction, FTIR, and X-ray photoelectron spectroscopy. *J Spectrosc* 2015;2015: 836859.
- [49] Dake LS, Baer DR, Zachara JM. Auger parameter measurements of zinc compounds relevant to zinc transport in the environment. *Surf Interface Anal* 1989;14:71–5.
- [50] Pederson LR. Two-dimensional chemical-state plot for lead using XPS. *J Electron Spectrosc Relat Phenom* 1982;28:203–9.
- [51] Rondon S, Sherwood PMA. Core level and valence band spectra of PbO by XPS. *Surf Sci Spectra* 1998;5:97–103.
- [52] Wagner CD. Chemical shifts of auger lines, and the auger parameter. *Faraday Discuss Chem Soc* 1975;60:291–300.
- [53] Burriesci N, Garbassi F, Petrera M, Petrini G. Influence of the bulk and surface properties on the performance of iron–antimony catalysts. *J Chem Soc Faraday Trans 1* 1982;78:817–33.
- [54] Carbuicchio M, Centi G, Forzatti P, Trifiro F, Villa PL. Propylene oxidation to acrolein on Fe–Sb–Ti–O catalysts. *J Catal* 1987;107:307–16.
- [55] Aso I, Furukawa S, Yamazoe N, Seiyama T. Catalytic properties of Fe2O3–Sb2O4 mixed oxides: I. Mechanism of propene oxidation. *J Catal* 1980;64:29–37.
- [56] Garbassi F. XPS and AES study of antimony oxides. *Surf Interface Anal* 1980;2: 165–9.
- [57] Izquierdo R, Sacher E, Yelon A. X-ray photoelectron spectra of antimony oxides. *Appl Surf Sci* 1989;40:175–7.
- [58] Liebig C, Paul S, Katryniok B, Guillon C, Couturier J-L, Dubois J-L, et al. Glycerol conversion to acrylonitrile by consecutive dehydration over WO3/TiO2 and ammoxidation over Sb–(Fe, V)–O. *Appl Catal B* 2013;132–133:170–82.
- [59] Allen MD, Poulston S, Bithell EG, Goringe MJ, Bowker M. An XPS, TEM, and TPD study of the oxidation and ammoxidation of propene using mixed Fe–Sb oxide catalysts. *J Catal* 1996;163:204–14.
- [60] Dong J, Chi Y, Tang Y, Ni M, Nzihou A, Weiss-Hortala E, et al. Partitioning of heavy metals in municipal solid waste pyrolysis, gasification, and incineration. *Energy Fuels* 2015;29:7516–25.
- [61] Pedersen AJ, van Lith SC, Frandsen FJ, Steinsen SD, Holgersen LB. Release to the gas phase of metals, S and Cl during combustion of dedicated waste fractions. *Fuel Process Technol* 2010;91:1062–72.
- [62] Lu P, Huang Q, Bourtsalas AC, Themelis NJ, Chi Y, Yan J. Review on fate of chlorine during thermal processing of solid wastes. *J Environ Sci* 2019;78:13–28.
- [63] Ma W, Wenga T, Frandsen FJ, Yan B, Chen G. The fate of chlorine during MSW incineration: vaporization, transformation, deposition, corrosion and remedies. *Prog Energy Combust Sci* 2020;76:100789.
- [64] Dayton DC, Milne TA. Laboratory measurements of alkali metal containing vapors released during biomass combustion. In: Baxter L, DeSollar R, editors. *Applications of Advanced Technology to Ash-Related Problems in Boilers*. Boston, MA: Springer, US; 1996. p. 161–85.
- [65] Knutsson P, Linderholm C. Characterization of ilmenite used as oxygen carrier in a 100 kW chemical-looping combustor for solid fuels. *Appl Energy* 2015;157: 368–73.
- [66] Dai J, Whitty K. Effects of coal ash on CuO as an oxygen carrier for chemical looping with oxygen uncoupling. *Energy Fuels* 2018;32:11656–65.
- [67] Durmaz M, Dilmaç N, Dilmaç ÖF. Evaluation of performance of copper converter slag as oxygen carrier in chemical-looping combustion (CLC). *Energy* 2020;196: 117055.



- [68] Darwish E, Yilmaz D, Leion H. Experimental and thermodynamic study on the interaction of copper oxygen carriers and oxide compounds commonly present in ashes. *Energy Fuels* 2019;33:2502–15.
- [69] Kuo Y-L, Huang W-C, Tseng Y-H, Chang S-H, Ku Y, Lee H-Y. Electric arc furnace dust as an alternative low-cost oxygen carrier for chemical looping combustion. *J Hazard Mater* 2018;342:297–305.
- [70] Elled A-L, Åmand L-E, Eskilsson D. Fate of zinc during combustion of demolition wood in a fluidized bed boiler. *Energy Fuels* 2008;22:1519–26.
- [71] Andersson C, Högberg J. Fouling and slagging problems at recovered wood fuel combustion. In: Värmforsk, editor. (in Swedish with English summary) ed. Stockholm2001.
- [72] Kinnunen H, Hedman M, Lindberg D, Enestam S, Yrjas P. Corrosion in recycled wood combustion—reasons, consequences, and solutions. *Energy Fuels* 2019;33: 5859–66.
- [73] Dai J, Hughey L, Whitty KJ. Influence of fuel ash on the recoverability of copper from the spent material of chemical looping combustion. *Fuel Process Technol* 2020;201:106358.